An Anti-Diffusive Numerical Scheme for the Simulation of Interfaces between Compressible Fluids by Means of a Five-Equation Model

F Lagoutière, Samuel Kokh

An Anti-Diffusive Numerical Scheme for the Simulation of Interfaces between Compressible Fluids by Means of a Five-Equation Model

S. Kokh[a,*], F. Lagoutière[b]

[a] *DEN/DANS/DM2S/SFME/LETR, CEA Saclay, 91191 Gif-sur-Yvette, Cedex, France.*
[b] *LJLL & Paris VII University, France.*

Abstract

We propose a discretization method of the five-equation model with isobaric closure presented in [2, 3] for the simulation of compressible two-phase flows with interfaces. This numerical solver is a Lagrange-Remap scheme that aims at controlling the numerical diffusion of the interface between both fluids thanks to the seminal ideas of [13, 6, 7]. This method does not involve any interface reconstruction procedure. The solver is equipped with built-in stability and consistency properties and is conservative with respect to mass, momentum, total energy and partial mass. This numerical scheme works with a very broad range of equations of state, including tabulated laws. Properties that ensure a good treatment of the Riemann invariants across the interface are demonstrated. As a consequence, the numerical method does not create spurious pressure oscillations at the interface. We show one-dimensional and two-dimensional classical numerical tests and comparisons with the classical upwind Lagrange-Remap approach.

Key words: two-phase flows, interface problems, anti-diffusive scheme

Contents

1 Introduction **1**

2 The Five-Equation System with Isobaric Closure **3**

3 Numerical Scheme **4**

3.1 General Quasi-Conservative Lagrange-Remap Form for the Five-Equation System 5

3.1.1 The System in Lagrangian Coordinates 5

3.1.2 The Lagrange-Remap Solver 5

3.1.3 Lagrange Step 7

3.1.4 Remap Step 7

3.2 Choice of the Flux $\widetilde{z}_{j+1/2}$ and Control of the Numerical Diffusion of the Interface 9

3.3 Trust Interval for $\widetilde{z}_{j+1/2}$ 10

*Corresponding author

3.3.1 Flux $\widetilde{z}_{j+1/2}$ Consistency Constraint for $\widetilde{z}_{j+1/2}$ . . . 10
3.3.2 Flux $\widetilde{y}_{j+1/2}$ Consistency Constraint for $\widetilde{z}_{j+1/2}$ . . . 10
3.3.3 Color Function Stability Constraint for $\widetilde{z}_{j+1/2}$ . . . 11
3.3.4 Mass Fraction Stability Constraint for $\widetilde{z}_{j+1/2}$ . . . 13
3.3.5 Existence of the Trust Interval . . . 15
3.4 Overall Algorithm . . . 16

4 Evolution of Constant Pressure and Velocity Profiles 17

5 Numerical Results 20

5.1 1D Advection Test . . . 20
5.2 Shock Tube Test . . . 24
5.3 Convergence Test . . . 26
5.4 2D Advection Test . . . 28
5.5 Shock/Bubble Interaction Test . . . 34
5.6 Kelvin-Helmoltz Test . . . 36

6 Conclusion 38

1. Introduction

The simulation of compressible two-phase flows with interfaces has received many contributions for the past years that popularized interface capture methods. For such methods the description of the interface between the fluids relies on a parameter generally called a color function. The color function can be a physically relevant parameter, e.g. a mass fraction of a volume fraction, or an abstract parameter that takes simply the value 0 (resp. 1) in fluid 0 (resp. 1). The ground of the interface capture methods consists in solving an evolution PDE for the color function without any interface reconstruction process. This usually creates a numerical transition zone for the color function that requires to introduce a mixture model. Indeed, when dealing with compressible fluids while we suppose both fluids to be equipped with their own Equation of State (EOS), no EOS is given *a priori* for the region where the interface becomes numerically smeared.

Among the numerous works that have addressed this issue we choose here to focus on the five-equation system proposed in [2, 3] that provides a convenient model for the EOS in the numerical transition zone. Let us mention that other five-equation systems have been studied by [14, 15, 18]. These works usually propose a discretization based on an approximate Riemann method. Unfortunately theses numerical solvers tend to extend the smeared zone that captures the interface. As a consequence, for simulations that require a relatively large amount of time steps the interface shape is no longer distinguishable. A possible cure for this drawback is to consider other interface capture methods such as the well-known level set methods [35, 23, 24, 8, 34, 33] which instrinsically do not smear the interface. Instead of capturing the profile of a

discontinuous color function, the level set methods propose to define the interface as the zero-level set of a function that approximates the signed distance to the interface in a neighbourhood of the latter. The implementation of a level set method consists then in following the evolution of the level set function thanks to a PDE instead of a discontinuous color function. However the level set methods does not ensure the resulting algorithm to be conservative in the general case and also require the use of additional treatment in order to reinitialize the level set function during the computation. Both of these issues have been widely examined by numerous works. Let us for example mention [36, 31, 37, 38, 30] for conservativity issues and the work of [16, 23, 17, 41, 28, 39] for reinitialization techniques.

An alternate approach to the problem of numerical inteface smearing has been considered by [7]. The core of the method relies on a stability analysis first developped for the simple case of the discretization of the linear advection equation [5, 13]. An extension to the capture of an interface for a specific multimaterial flow model was then derived in [7] by means of a Lagrange-Remap strategy.

Following the way paved by [13, 6, 7] the present paper proposes a Lagrange-Remap solver for the five-equation model of [2, 3] that complies with the following constraint: the solver in conservative in partial masses, momentum, density and total energy. Moreover one can show that for a wide range of flow configurations the solver will provide stability for both mass fraction and color function, at least as well as the classical upwind solver. The solver also provides a good treatment of the Riemann invariants across the material front in a similar way to the the solver proposed in [2, 3]. Let us also emphasize that our scheme does not require any additional CPU cost compared to a classical upwind Lagrange-Remap method.

The overall construction principle of our numerical scheme has been presented in [32] along with a few preliminary simulations. We intend to provide here a thorough presentation of this numerical scheme and its properties, as well as detailed numerical results. The paper is organized as follows: in the first section we recall the five-equation model with isobaric closure of [2, 3] along with its main properties, then in section 3.1.2 we recall the general structure of a Lagrange-Remap solver. In the section 3.1.4 we show that, following our lines, the design of the whole solver boils down to properly define a numerical flux for the color function. This matter is examined in section 3.2 where we provide stability and consistency constraints for the numerical flux associated with the color function and shows that all of theses constraints are compatible with each other. In section 3.4 we present the full algorithm. We examine section 4 the effect of our scheme on the Riemann invariants across the interface. Finally, we present in section 5 a series of 1D and 2D numerical tests that show the good behaviour of the scheme regarding the numerical diffusion of the interface.

2. The Five-Equation System with Isobaric Closure

We briefly recall in this section the system we are concerned with and its main properties. The notations we shall use here slightly differ from the original notations of [2, 3].

We note ρ_k, ε_k and P_k respectively the density, the specific internal energy and the pressure of fluid $k = 0, 1$. We suppose each fluid $k = 0, 1$ to be equipped with an equation of state (EOS) of the form $\rho_k\varepsilon_k : (\rho_k, P_k) \mapsto \rho_k\varepsilon_k$. The position of the interface is located thanks to a color function $(x, t) \mapsto z$ that takes the value 1 (resp. 0) when the point x belongs to a pure fluid 1 (resp. 0) region at instant t.

The density ρ and specific energy ε of the two-fluid medium are given by

$$\rho = z\rho_1 + (1 - z)\rho_0, \qquad \rho\varepsilon = z\rho_1\varepsilon_1 + (1 - z)\rho_0\varepsilon_0.$$

We define the mass fraction y_k of the fluid $k = 0, 1$ by setting

$$y = z\rho_1/\rho, \qquad y_1 = y, \qquad y_0 = 1 - y.$$

Both fluids are supposed to have the same velocity $\mathbf{u}$ and we note $e = \varepsilon + |\mathbf{u}|^2/2$ the specific total energy of the two-fluid medium. For $k = 0, 1$ let us also note $\xi_k = (\partial\rho_k\varepsilon_k/\partial P_k)_{\rho_k}$ and c_k the sound velocity of pure fluid k assumed to be real valued. The five-equation system with isobaric closure reads

$$\left\{\begin{array}{r} \dfrac{\partial \rho y}{\partial t} + \operatorname{div}(\rho y \mathbf{u}) = 0, \\ \dfrac{\partial \rho}{\partial t} + \operatorname{div}(\rho \mathbf{u}) = 0, \\ \dfrac{\partial \rho \mathbf{u}}{\partial t} + \mathbf{div}(\rho \mathbf{u} \otimes \mathbf{u}) + \mathbf{grad} P = 0, \\ \dfrac{\partial \rho e}{\partial t} + \operatorname{div}[(\rho e + P)\mathbf{u}] = 0, \\ \dfrac{\partial z}{\partial t} + \mathbf{u} \cdot \mathbf{grad} z = 0, \end{array}\right. \tag{1}$$

where the pressure law $P : (\rho_0(1 - z), \rho_1 z, \rho\varepsilon, z) \mapsto P$ is defined as the solution of the system

$$\left\{\begin{array}{l} P = P_1(\rho_1, \rho_1\varepsilon_1) = P_0(\rho_0, \rho_0\varepsilon_0), \\ \rho\varepsilon = z\rho_1\varepsilon_1 + (1 - z)\rho_0\varepsilon_0, \end{array}\right. \tag{2}$$

for given values of ρ_0, ρ_1, z and ε. The system (2) provides a consistent definition of P for a very wide class of fluids. Indeed, one can state that if each pure fluid $k = 0, 1$ EOS verifies

$$\xi_k > 0, \qquad P_k \geq 0, \qquad (\rho_k, \rho_k\varepsilon_k) \mapsto P_k \text{ is a } \mathscr{C}^1 \text{ function such that } P_k(\rho_k, \rho_k\varepsilon_k = 0) = 0,$$

then (2) always has a single solution (see [2, 3]). Moreover, for very fluids such as Mie-Gruneisen materials, van der Waals fluids, stiffened gases or perfect gases, the system (2) always admits a solution P that can be expressed explicitly by means of the variables ρ_0, ρ_1, z and ε. Let us note that solving (2) also enables to retrieve the phasic energies $\rho_k\varepsilon_k$ thanks to the pure fluids EOS by setting $\rho_k\varepsilon_k = \rho_k\varepsilon_k(\rho_k, P)$, where P is the solution of (2), for $k = 0, 1$.

Remark 1. *When $z = 0$ (resp. $z = 1$), the closure law defined by* (2) *may be ambiguous as ρ_1 (resp. ρ_0) becomes an arbitrary parameter. In this case, we use a threshold value $\eta > 0$ as follows: when $z < \eta$ (resp.*

$1-\eta < z$) we set $P = P_0(\rho, \rho\varepsilon)$ (resp. $P = P_1(\rho, \rho\varepsilon)$). When $\eta < z < 1-\eta$ we retrieve P by solving (2). In practice we use $\eta = 10^{-5}$, but we did not experience a great sensitivity of the simulation results when choosing smaller values for η. Let us also note that for stiffened gases or perfect gases, the explicit definition of P degenerates naturally when z tends to 0 (resp. 1), therefore in these cases no threshold is needed.

Let us now briefly recall the eigenstructure of the five-equation system with isobaric closure. For one-dimensional problems, smooth solutions of the system (1) verify the following quasi-linear system

$$\partial_t \begin{bmatrix} \rho\mathbf{V} \\ z \end{bmatrix} + A(\rho\mathbf{V}, z)\partial_x \begin{bmatrix} \rho\mathbf{V} \\ z \end{bmatrix} = 0, \quad \rho\mathbf{V} = (\rho y, \rho, \rho u, \rho e)^T. \tag{3}$$

We now recall the main well-posedness property of the system (3).

Proposition 2.1. *Suppose that $\xi_1 > 0$ and $\xi_2 > 0$, then the matrix $A(\rho\mathbf{V}, z)$ possesses 5 real eigenvalues $\{u-c, u, u, u, u+c\}$, where the sound velocity c of the system (3) verifies*

$$\xi = z\xi_1 + (1-z)\xi_0, \qquad \rho\xi c^2 = z\rho_1\xi_1 c_1^2 + (1-z)\rho_0\xi_0 c_0^2.$$

Moreover the matrix $A(\rho\mathbf{V}, z)$ also possesses a set of eigenvectors that spans $\mathbb{R}^5$. Therefore the system (3) is hyperbolic. The fields associated with the eigenvalues $u \pm c$ are genuinely nonlinear and the fields associated with the eigenvalues u are linearly degenerate.

Remark 2. The system (1) can be expressed in an equivalent fully conservative form using the variables $(\rho y, \rho, \rho\mathbf{u}, \rho e, \rho z)^T$. Indeed, the variable z is only allowed to experience a jump in its value across the material interface which is associated with the linearly degenerate field. This ensures that the non-conservative product $\mathbf{u} \cdot \mathrm{grad} z$ is unambiguously defined and that the advection equation for z in system (1) can be replaced by the conservation equation: $\partial_t(\rho z) + \mathrm{div}(\rho z\mathbf{u}) = 0$.

In the sequel we shall always suppose the EOS of both fluids to match hypotheses that guarantee hyperbolicity for the system (3) and that provide a consistent definition of the pressure P. More specifically we shall assume that for any given values of $\rho_0 > 0$, $\rho_1 > 0$, $0 < z < 1$ and $\varepsilon > 0$, there is a single pressure P verifying the isobaric closure (2) and singled defined phasic energies $\rho_1\varepsilon_1$ and $\rho_0\varepsilon_0$ such that $\rho\varepsilon = z\rho_1\varepsilon_1 + (1-z)\rho_0\varepsilon_0$.

3. Numerical Scheme

This section is the very core of our work. We first present a general structure for the algorithm by recalling the Lagrange-Remap process for the special case of the five-equation system with isobaric closure. While the Lagrange step is standard, we shall detail how to build a convenient Remap step that ensures some consistency and stability properties for the scheme and also allows to minimize the diffusion of the variables that help to locate the interface.

3.1. General Quasi-Conservative Lagrange-Remap Form for the Five-Equation System

3.1.1. The System in Lagrangian Coordinates

Let us first recall the expression of system (3) in Lagrangian coordinates. If we note $\mathrm{D}_t \cdot = \partial_t \cdot + u\partial_x \cdot$ the material derivative, then considering smooth solutions the system (3) also reads

$$\begin{aligned} \rho \mathrm{D}_t y &= 0, \\ \rho \mathrm{D}_t \tau - \partial_x u &= 0, \\ \rho \mathrm{D}_t u + \partial_x P &= 0, \\ \rho \mathrm{D}_t e + \partial_x (Pu) &= 0, \\ \rho \mathrm{D}_t z &= 0, \end{aligned} \tag{4}$$

where $\tau = 1/\rho$. The Lagrangian coordinates system (X, t) attached to the initial instant $t = 0$ is defined by

$$X = \chi^{-1}(x,t), \qquad \begin{cases} \dfrac{\partial}{\partial t}\chi(X,t) = u(\chi(X,t),t), \\ \chi(X, t=0) = X, \end{cases} \tag{5}$$

which states that $x = \chi(X, t)$ is the position at time t of the particle that was at the coordinates X at instant $t = 0$. Equivalently we can say that $X = \chi^{-1}(x, t)$ is the initial position at $t = 0$ of the particle that is located at the position x at the instant t. If one considers any Eulerian field $q : (x, t) \mapsto q$, then we can define a Lagragian field $q^{\mathrm{Lag}} : (X, T) \mapsto q^{\mathrm{Lag}}(X, t)$ by setting $q^{\mathrm{Lag}}(X, t) = q(\chi(X, t), t)$. Using this notation the system (4) is thus equivalent to

$$\begin{aligned} \rho^{\mathrm{Lag}} \partial_t y^{\mathrm{Lag}} &= 0, \\ \rho^{\mathrm{Lag}} \partial_t \tau^{\mathrm{Lag}} - \partial_X u^{\mathrm{Lag}} &= 0, \\ \rho^{\mathrm{Lag}} \partial_t u^{\mathrm{Lag}} + \partial_X P^{\mathrm{Lag}} &= 0, \\ \rho^{\mathrm{Lag}} \partial_t e^{\mathrm{Lag}} + \partial_X (P^{\mathrm{Lag}} u^{\mathrm{Lag}}) &= 0, \\ \rho^{\mathrm{Lag}} \partial_t z^{\mathrm{Lag}} &= 0. \end{aligned} \tag{6}$$

3.1.2. The Lagrange-Remap Solver

We are now able to recall the Lagrange-Remap procedure. For a general presentation of this algorithm the reader can refer to [9]. Let us introduce some classical notations: let $q : (x, t) \mapsto q(x, t)$ be any Eulerian field, we denote by q_j^n an approximate value of

$$\frac{1}{\Delta x} \int_{x_{j-1/2}}^{x_{j+1/2}} q(x, t^n) \mathrm{d}x, \quad j \in \mathbb{Z}, n \in \mathbb{N},$$

where Δx is the space step and $x_j = j\Delta x$, $x_{j+1/2} = (j + 1/2)\Delta x$. The real interval $[x_{j-1/2}, x_{j+1/2}]$ will be refered to as cell j, or cell centered in x_j. We shall note $(q_j^n)_{j\in\mathbb{Z}} = (q^n)$.

We consider a single time step from the instant t^n to the instant t^{n+1}. Let $(\rho^n \mathbf{V}^n, z^n)$ be the discretized state variable at time t^n. The Lagrange-Remap solver consists in performing the three following steps (see figure 1).

Step 1. Consider a Lagrangian coordinates system attached to instant $t = t^n$. Build the discretized Lagrangian variable $(\rho^{\mathrm{Lag}} \mathbf{V}^{\mathrm{Lag}}, z^{\mathrm{Lag}}) = (\rho^n \mathbf{V}^n, z^n)$ associated with the discrete Eulerian $(\rho^n \mathbf{V}^n, z^n)$ state variable at time t^n.

Step 2. Update the Lagrangian variable $(\rho^{\mathrm{Lag}} \mathbf{V}^{\mathrm{Lag}}, z^{\mathrm{Lag}})$ to the its state $(\widetilde{\rho}\widetilde{\mathbf{V}}, \widetilde{z})$ at instant $t = t^{n+1}$ by solving numerically the system (6).

Step 3. Remap the Lagrangian variable $(\widetilde{\rho}\widetilde{\mathbf{V}}, \widetilde{z})$ onto the Eulerian mesh which provides the discretized Eulerian variable $(\rho^{n+1}\mathbf{V}^{n+1}, z^{n+1})$ at time $t = t^{n+1}$, by solving numerically the system (6). This step is equivalent to account for the fact that the mesh associated with the Lagrangian system is deformed by (5) through the resolution of (6) from t^n to t^{n+1}.

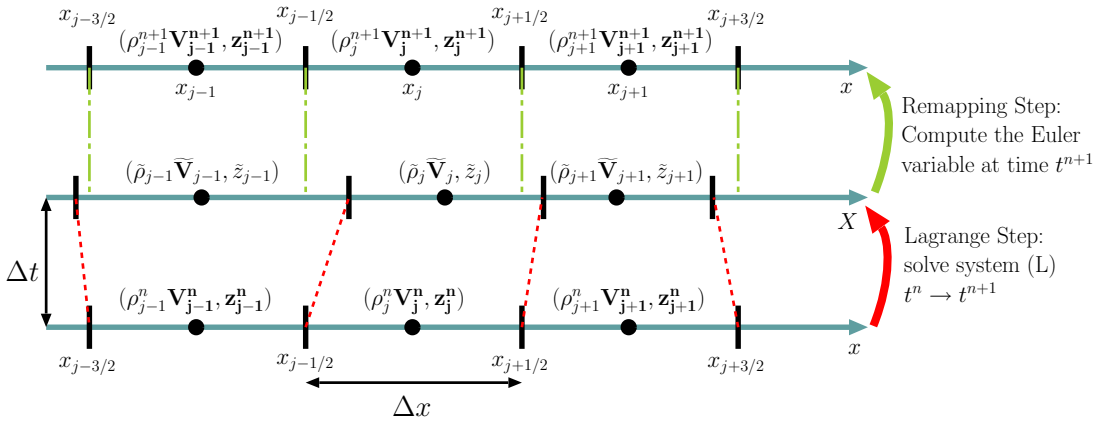

Figure 1: Structure of the Lagrange-Remap numerical scheme.

As it will be shown in section 3.4, a simple equation substition allows to see that the overall algorithm can be put in conservative form for the variables ρ, ρy, ρu and ρe.

For the sake of readability, we shall use the following notations throughout the present work: for $j \in \mathbb{Z}$ and $n \in \mathbb{N}$

- q_j^n is an approximate value of the field q in the Eulerian frame within the cell j at instant t^n,
- $q_{j+1/2}$ is an approximate value of the field q in the Eulerian frame at the interface $j+1/2$ that separates the cell j and the cell $j+1$ at instant t^n,
- $\widetilde{q}_j$ is an approximate value of the field q in the Lagrangian frame within the cell j at instant t^{n+1},

- $\widetilde{q}_{j+1/2}$ is an approximate value of the field q in the Lagrangian frame at the interface $j+1/2$ that separates the cell j and the cell $j+1$ at instant t^{n+1}.

3.1.3. Lagrange Step

The step 2 is a simple discretization of (6). Following the same lines as in [7] we use here the so-called "acoustic scheme" [4] that reads

$$\left\{\begin{array}{r} \widetilde{y}_j = y_j^n, \\ \widetilde{z}_j = z_j^n, \\ \rho_j^n \dfrac{\widetilde{\tau}_j - \tau_j^n}{\Delta t} - \dfrac{1}{\Delta x}\Big(u_{j+1/2} - u_{j-1/2}\Big) = 0, \\ \rho_j^n \dfrac{\widetilde{u}_j - u_j^n}{\Delta t} + \dfrac{1}{\Delta x}\Big(P_{j+1/2} - P_{j-1/2}\Big) = 0, \\ \rho_j^n \dfrac{\widetilde{e}_j - e_j^n}{\Delta t} + \dfrac{1}{\Delta x}\Big(P_{j+1/2}u_{j+1/2} - P_{j-1/2}u_{j-1/2}\Big) = 0, \end{array}\right. \tag{7}$$

where the numerical fluxes are defined with

$$\left\{\begin{array}{l} u_{j+1/2} = \dfrac{1}{2}(u_{j+1} + u_j) - \dfrac{1}{2(\rho c)_{j+1/2}}(P_{j+1} - P_j), \\ P_{j+1/2} = \dfrac{1}{2}(P_{j+1} + P_j) - \dfrac{(\rho c)_{j+1/2}}{2}(u_{j+1} - u_j), \\ (\rho c)_{j+1/2} = \sqrt{\max(\rho_{j+1}c_{j+1}^2, \rho_j c_j^2)\min(\rho_{j+1}, \rho_j)}. \end{array}\right. \tag{8}$$

The time step Δt is chosen in agreement with the following CFL condition

$$\frac{\Delta t}{\Delta x}\max_{j\in\mathbb{Z}}\big(|u_{j+1/2}|, (\rho c)_{j+1/2}/\min(\rho_j^n, \rho_{j+1}^n)\big) \leq C^{\mathrm{CFL}}, \tag{9}$$

with C^{CFL} usually chosen close to 0.8. The stability of the Lagrange step (7) under the condition (9) has been investigated in [4].

Let us now turn to the step 3.

3.1.4. Remap Step

The procedure of remapping the Lagrangian variable onto the Eulerian mesh consists in a discrete resolution of the system (5). Following classical lines (see *eg* [9]) we choose for this step a discretization of the form

$$\left\{\begin{array}{r} \dfrac{\rho_j^{n+1} - \rho_j^n}{\Delta t} + \dfrac{1}{\Delta x}\Big(\widetilde{\rho}_{j+1/2}u_{j+1/2} - \widetilde{\rho}_{j-1/2}u_{j-1/2}\Big) = 0, \\ \dfrac{\rho_j^{n+1}y_j^{n+1} - \rho_j^n\widetilde{y}_j}{\Delta t} + \dfrac{1}{\Delta x}\Big(\widetilde{\rho}_{j+1/2}\widetilde{y}_{j+1/2}u_{j+1/2} - \widetilde{\rho}_{j-1/2}\widetilde{y}_{j-1/2}u_{j-1/2}\Big) = 0, \\ \dfrac{\rho_j^{n+1}u_j^{n+1} - \rho_j^n\widetilde{u}_j}{\Delta t} + \dfrac{1}{\Delta x}\Big(\widetilde{\rho}_{j+1/2}\widetilde{u}_{j+1/2}u_{j+1/2} - \widetilde{\rho}_{j-1/2}\widetilde{u}_{j-1/2}u_{j-1/2}\Big) = 0, \\ \dfrac{\rho_j^{n+1}e_j^{n+1} - \rho_j^n\widetilde{e}_j}{\Delta t} + \dfrac{1}{\Delta x}\Big(\widetilde{\rho}_{j+1/2}\widetilde{e}_{j+1/2}u_{j+1/2} - \widetilde{\rho}_{j-1/2}\widetilde{e}_{j-1/2}u_{j-1/2}\Big) = 0, \\ \dfrac{z_j^{n+1} - z_j^n}{\Delta t} + \dfrac{1}{\Delta x}\Big(\widetilde{z}_{j+1/2}u_{j+1/2} - \widetilde{z}_{j-1/2}u_{j-1/2}\Big) - \dfrac{1}{\Delta x}z_j^n\Big(u_{j+1/2} - u_{j-1/2}\Big) = 0. \end{array}\right. \tag{10}$$

The update (10) from $(\widetilde{\rho}\widetilde{\mathbf{V}}, \widetilde{z})$ to $(\rho^{n+1}\mathbf{V}^{n+1}, z^{n+1})$ is consistant with an advection step. Let us emphasize that (10) clearly shows a conservative discretization for the variables $\rho\mathbf{V}$ and a non-conservative discretization for z. Once again, the time step Δt is chosen according to the CFL condition (9), which ensures stability.

Given the Lagrange step described in section 3.1.3 and given the canevas (10) we only need to specify the numerical flux $(\widetilde{\rho}\widetilde{\mathbf{V}}, \widetilde{z})_{j+1/2}$ in order to obtain a fully defined Remap Step and therefore a fully defined Lagrange-Remap scheme. Consequently, building the numerical scheme boils down to define

$$\widetilde{y}_{j+1/2}, \qquad \widetilde{\rho}_{j+1/2}, \qquad \widetilde{u}_{j+1/2}, \qquad \widetilde{z}_{j+1/2}, \qquad \widetilde{(\rho\varepsilon)}_{j+1/2}, \qquad \widetilde{z}_{j+1/2}. \tag{11}$$

We propose to choose the quantities in (11) as follows: first, we enforce the flux consistency for y, ρ and ε by setting

$$\begin{aligned} \widetilde{y}_{j+1/2} &= \frac{\widetilde{z}_{j+1/2}\widetilde{(\rho_1)}_{j+1/2}}{\widetilde{\rho}_{j+1/2}}, \\ \widetilde{\rho}_{j+1/2} &= \widetilde{z}_{j+1/2}\widetilde{(\rho_1)}_{j+1/2} + (1-\widetilde{z}_{j+1/2})\widetilde{(\rho_0)}_{j+1/2}, \\ \widetilde{\rho}_{j+1/2}\widetilde{\varepsilon}_{j+1/2} &= \widetilde{z}_{j+1/2}\widetilde{(\rho_1\varepsilon_1)}_{j+1/2} + (1-\widetilde{z}_{j+1/2})\widetilde{(\rho_0\varepsilon_0)}_{j+1/2}. \end{aligned} \tag{12}$$

The definition of the terms in (11) now boils down to choose the following fluxes

$$\widetilde{(\rho_0)}_{j+1/2}, \qquad \widetilde{(\rho_1)}_{j+1/2}, \qquad \widetilde{(\rho_0\varepsilon_0)}_{j+1/2}, \qquad \widetilde{(\rho_1\varepsilon_1)}_{j+1/2}, \qquad \widetilde{u}_{j+1/2}, \qquad \widetilde{z}_{j+1/2}.$$

For $\widetilde{(\rho_k)}_{j+1/2}$, $\widetilde{(\rho_k\varepsilon_k)}_{j+1/2}$ and $\widetilde{u}_{j+1/2}$ we choose the upwind value according the sign of the interface velocity $u_{j+1/2}$, namely

$$(\widetilde{\rho}_0, \widetilde{\rho}_1, \widetilde{\rho_0\varepsilon_0}, \widetilde{\rho_1\varepsilon_1}, \widetilde{u})_{j+1/2} = \begin{cases} (\widetilde{\rho}_0, \widetilde{\rho}_1, \widetilde{\rho_0\varepsilon_0}, \widetilde{\rho_1\varepsilon_1}, \widetilde{u})_j & \text{if } u_{j+1/2} > 0 \\ (\widetilde{\rho}_0, \widetilde{\rho}_1, \widetilde{\rho_0\varepsilon_0}, \widetilde{\rho_1\varepsilon_1}, \widetilde{u})_{j+1} & \text{if } u_{j+1/2} < 0 \end{cases}. \tag{13}$$

Finally, given the choices (13) and (12) we are only left with the problem of choosing the value of $\widetilde{z}_{j+1/2}$. This task is the purpose of the next sections 3.3.1, 3.3.2, 3.3.3, 3.3.4 and 3.2. When we settle on this point, the numerical scheme will be fully defined.

3.2. Choice of the Flux $\widetilde{z}_{j+1/2}$ and Control of the Numerical Diffusion of the Interface

As it has been made clear in section 3.1.4, we only need to define the numerical flux $\widetilde{z}_{j+1/2}$ at each cell interface $j+1/2$ in order to complete the construction of the numerical scheme. For the sake of clarity we anticipate the results of the section 3.3 and we propose in the present section some general guidelines inspired from [5, 13, 7]. These guidelines will allow us to choose $\widetilde{z}_{j+1/2}$ so that the material interface remains as sharp as possible throughout the computation.

Let us suppose that we know a sequence of real intervals $(I_{j+1/2})_{j\in\mathbb{Z}}$ that shall be referred to as "trust intervals" in the sequel. These intervals are such that, for a given $j \in \mathbb{Z}$, if the flow variable $(\rho\mathbf{V}, z)^n$ matches a certain flow configuration $C_{j+1/2}$ in the neighbouring cells of the interface $j+1/2$ then $\widetilde{z}_{j+1/2} \in I_{j+1/2}$

implies that the scheme fulfills numerical features such as consistency and stability in some sense. Then we propose to choose $\widetilde{z}_{j+1/2}$ according to the following strategy.

a°) If the flow $(\rho\mathbf{V}, z)^n$does not match the flow configuration $C_{j+1/2}$ in a neighbourhood of the interface $j+1/2$, then we choose $\widetilde{z}_{j+1/2}$ as the upwind value of $z^n = \widetilde{z}$ according to the sign of $u_{j+1/2}$.

b°) If the flow $(\rho\mathbf{V}, z)^n$ does match the flow configuration $C_{j+1/2}$ in a neighbourhood of the interface $j+1/2$, then we choose $\widetilde{z}_{j+1/2}$ such that it belongs to $I_{j+1/2}$ and such that $\widetilde{z}_{j+1/2}$ is as close as possible to the downwind value of $\widetilde{z} = z^n$ according to the sign of $u_{j+1/2}$.

This strategy means that when the trust interval $I_{j+1/2}$ provides stability and consistency, we choose $\widetilde{z}_{j+1/2}$ "as downwind as possible" within $I_{j+1/2}$, when $I_{j+1/2}$ does not give any information about the choice of $\widetilde{z}_{j+1/2}$ we choose the upwind value as a "safety measure".

In the sequel we shall see that the flow configurations $C_{j+1/2}$ we shall take into account simply relates to the sign of $u_{j+1/2}$, $u_{j-1/2}$ and $u_{j+3/2}$. Moreover, the next sections will allow us to build a trust interval $I_{j+1/2}$ that provides

- consistency for the flux $\widetilde{z}_{j+1/2}$ (see section 3.3.1),
- consistency for the flux $\widetilde{y}_{j+1/2}$ (see section 3.3.2),
- stability for variable z (see section 3.3.3),
- stability for variable y (see section 3.3.4).

Let us emphasize that thanks to this list of features, despite that $\widetilde{z}_{j+1/2}$ is chosen downwind or as close as possible to the downwind value our scheme is endowed with good stability and consistency properties. This downwind choice constrained by stability and consistency will prevent the interface from being smeared by the numerical scheme as in [5, 13, 6, 7].

The sections 3.3.1, 3.3.2, 3.3.3 and 3.3.4 are dedicated to the detailed derivation of the trust intervals $I_{j+1/2}$ and the overall algorithm is described in section 3.4.

3.3. Trust Interval for $\widetilde{z}_{j+1/2}$

Before going any further we introduce the following notations

$$m_{j+1/2} = \min(z_j^n, z_{j+1}^n), \qquad M_{j+1/2}(y) = \max(z_j^n, z_{j+1}^n),$$
$$\mathfrak{m}_{j+1/2} = \min(y_j^n, y_{j+1}^n), \qquad \mathfrak{M}_{j+1/2}(y) = \max(y_j^n, y_{j+1}^n).$$

We suppose that $0 \leq z_j^n \leq 1$ and $0 \leq y_j^n \leq 1$ for all $j \in \mathbb{Z}$, which implies that $m_{j+1/2}$, $M_{j+1/2}$, $\mathfrak{m}_{j+1/2}$ and $\mathfrak{M}_{j+1/2}$ belong to the interval $[0,1]$ for all $j \in \mathbb{Z}$. Moreover we make the assumption that

$$\widetilde{(\rho_0)}_{j+1/2} > 0 \quad \text{and} \quad \widetilde{(\rho_1)}_{j+1/2} > 0, \quad \forall j \in \mathbb{Z}, \tag{14}$$

and that Δt and Δx satisfy the CFL condition (9).

3.3.1. Flux $\widetilde{z}_{j+1/2}$ Consistency Constraint for $\widetilde{z}_{j+1/2}$

As in [5, 13, 7] we remark that as soon as $m_{j+1/2} \leq \widetilde{z}_{j+1/2} \leq M_{j+1/2}$ then the flux $\widetilde{z}_{j+1/2}$ is consistent. Therefore there is a "trust interval" $[m_{j+1/2}, M_{j+1/2}]$ for $\widetilde{z}_{j+1/2}$ that ensures the consistency of the flux for the variable z in the sense that

$$\widetilde{z}_{j+1/2} \in [m_{j+1/2}, M_{j+1/2}] \Longrightarrow \text{ consistency for } \widetilde{z}_{j+1/2}. \tag{15}$$

In the following, we shall consider $\widetilde{z}_{j+1/2} \in [m_{j+1/2}, M_{j+1/2}]$, for all $j \in \mathbb{Z}$.

3.3.2. Flux $\widetilde{y}_{j+1/2}$ Consistency Constraint for $\widetilde{z}_{j+1/2}$

In a similar way to in the previous section, we note that as soon as $\mathfrak{m}_{j+1/2} \leq \widetilde{y}_{j+1/2} \leq \mathfrak{M}_{j+1/2}$ then the flux $\widetilde{y}_{j+1/2}$ for the variable y is consistent. Using the definition (12), we see that $\mathfrak{m}_{j+1/2} \leq \widetilde{y}_{j+1/2}$ is equivalent to

$$\mathfrak{m}_{j+1/2} \leq \frac{\widetilde{(\rho_1)}_{j+1/2}\widetilde{z}_{j+1/2}}{\widetilde{z}_{j+1/2}\widetilde{(\rho_1)}_{j+1/2} + (1-\widetilde{z}_{j+1/2})\widetilde{(\rho_0)}_{j+1/2}}, \tag{16}$$

which also reads

$$\widetilde{z}_{j+1/2}\left\{\widetilde{(\rho_1)}_{j+1/2}(1-\mathfrak{m}_{j+1/2}) + \widetilde{(\rho_0)}_{j+1/2}\mathfrak{m}_{j+1/2}\right\} \geq \widetilde{(\rho_0)}_{j+1/2}\mathfrak{m}_{j+1/2}.$$

According to the hypotheses presented at the beginning of the section 3.3, we see that $\widetilde{(\rho_1)}_{j+1/2}(1-\mathfrak{m}_{j+1/2}) + \widetilde{(\rho_0)}_{j+1/2}\mathfrak{m}_{j+1/2} > 0$ and therefore (16) is equivalent to

$$\frac{\widetilde{(\rho_0)}_{j+1/2}\mathfrak{m}_{j+1/2}}{\widetilde{(\rho_1)}_{j+1/2}(1-\mathfrak{m}_{j+1/2}) + \widetilde{(\rho_0)}_{j+1/2}\mathfrak{m}_{j+1/2}} \leq \widetilde{z}_{j+1/2}.$$

Using the same lines we see that an equivalent condition for $\widetilde{z}_{j+1/2}$ to be such that $\widetilde{y}_{j+1/2} \leq \mathfrak{M}_{j+1/2}$ is

$$\widetilde{z}_{j+1/2} \leq \frac{\widetilde{(\rho_0)}_{j+1/2}\mathfrak{M}_{j+1/2}}{\widetilde{(\rho_1)}_{j+1/2}(1-\mathfrak{M}_{j+1/2}) + \widetilde{(\rho_0)}_{j+1/2}\mathfrak{M}_{j+1/2}}.$$

Then if we note

$$d_{j+1/2} = \frac{\widetilde{(\rho_0)}_{j+1/2}\mathfrak{m}_{j+1/2}}{\widetilde{(\rho_1)}_{j+1/2}(1-\mathfrak{m}_{j+1/2}) + \widetilde{(\rho_0)}_{j+1/2}\mathfrak{m}_{j+1/2}}, \tag{17}$$

$$D_{j+1/2} = \frac{\widetilde{(\rho_0)}_{j+1/2}\mathfrak{M}_{j+1/2}}{\widetilde{(\rho_1)}_{j+1/2}(1-\mathfrak{M}_{j+1/2}) + \widetilde{(\rho_0)}_{j+1/2}\mathfrak{M}_{j+1/2}}, \tag{18}$$

we see that $[d_{j+1/2}, D_{j+1/2}]$ is a trust interval for $\widetilde{z}_{j+1/2}$ that ensures consistency for the flux $\widetilde{y}_{j+1/2}$ in the sense that

$$\widetilde{z}_{j+1/2} \in [d_{j+1/2}, D_{j+1/2}] \Longrightarrow \widetilde{y}_{j+1/2} \in [\mathfrak{m}_{j+1/2}, \mathfrak{M}_{j+1/2}] \Longrightarrow \text{consistency for } \widetilde{y}_{j+1/2}.$$

In the sequel, we shall consider that $\widetilde{z}_{j+1/2} \in [d_{j+1/2}, D_{j+1/2}]$, for all $j \in \mathbb{Z}$. We assume that this ansatz is compatible with $\widetilde{z}_{j+1/2} \in [m_{j+1/2}, M_{j+1/2}]$, however this point will be proven in section 3.3.5.

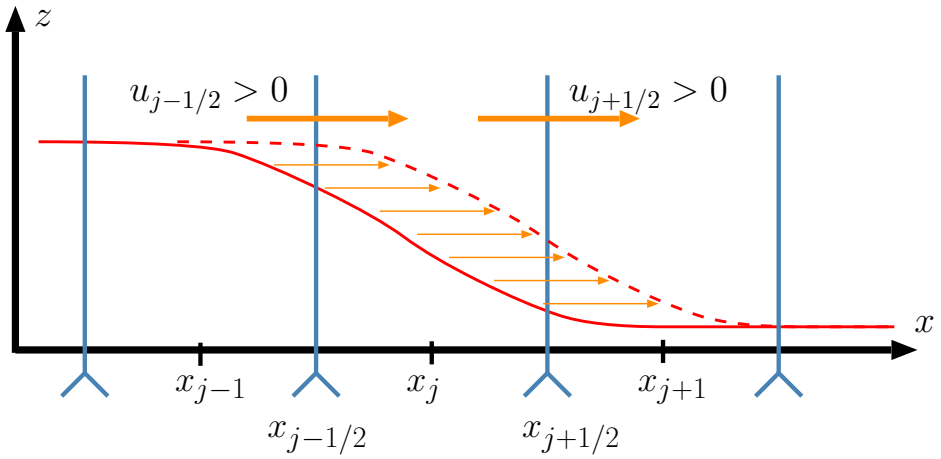

Figure 2: Condition for the z-stability: for the configuration $u_{j+1/2} > 0$ and $u_{j-1/2} > 0$, the stability is ensured by $m_{j-1/2} \leq z_j^{n+1} \leq M_{j-1/2}$.

3.3.3. Color Function Stability Constraint for $\widetilde{z}_{j+1/2}$

In the present section we shall exhibit a condition on $\widetilde{z}_{j+1/2}$ that ensures stability for the variable z in a neighbour cell of the interface $j+1/2$ when the velocities at the interfaces of this cell have the same sign. More precisely, one considers the cell whose z value is "emptied" by the flux $\widetilde{z}_{j+1/2}$, namely the cell j (resp. cell $j+1$) when $u_{j+1/2} > 0$ and $u_{j-1/2} > 0$ (resp. $u_{j+1/2} < 0$ and $u_{j+3/2} < 0$). Then we seek a sufficient condition that enforces a local maximum principle in the cell j (resp. cell $j+1$).

Suppose that $u_{j+1/2} > 0$ and $u_{j-1/2} > 0$. In this particular flow configuration for the cell j, we have a very simple sufficient stability condition for z_j

$$m_{j-1/2} \leq z_j^{n+1} \leq M_{j-1/2} \Longrightarrow \text{ stability for } z \text{ in the cell } j. \tag{19}$$

We shall now seek conditions on $\widetilde{z}_{j+1/2}$ that ensures $z_j^{n+1} \in [m_{j-1/2}, M_{j-1/2}]$. According to (10), a sufficient condition for $m_{j-1/2} \leq z_j^{n+1}$ is given by

$$m_{j-1/2} \leq z_j^n - \frac{\Delta t}{\Delta x}\Big(\widetilde{z}_{j+1/2}u_{j+1/2} - \widetilde{z}_{j-1/2}u_{j-1/2}\Big) + \frac{\Delta t}{\Delta x} z_j^n \Big(u_{j+1/2} - u_{j-1/2}\Big),$$

which also reads

$$\frac{\Delta x}{\Delta t}(m_{j-1/2} - z_j^n) - z_j^n\Big(u_{j+1/2} - u_{j-1/2}\Big) - \widetilde{z}_{j-1/2}u_{j-1/2} \leq -\widetilde{z}_{j+1/2}u_{j+1/2}. \tag{20}$$

As $\widetilde{z}_{j-1/2}$ is chosen within the consistency trust interval $[m_{j-1/2}, M_{j-1/2}]$, we have $-\widetilde{z}_{j+1/2} \leq -m_{j-1/2}^n$, consequently a sufficient condition for (20) to be satisfied is

$$\frac{\Delta x}{\Delta t}(m_{j-1/2} - z_j^n) - z_j^n\Big(u_{j+1/2} - u_{j-1/2}\Big) - m_{j-1/2}u_{j-1/2} \leq -\widetilde{z}_{j+1/2}u_{j+1/2},$$

and equivalently

$$\widetilde{z}_{j+1/2} \leq z_j^n + (m_{j-1/2} - z_j^n)\left(\frac{u_{j-1/2}}{u_{j+1/2}} - \frac{\Delta x}{\Delta t}\frac{1}{u_{j+1/2}}\right). \tag{21}$$

Symmetrically, we see that a sufficient condition for $\widetilde{z}_{j+1/2}$ to be such that $z_j^{n+1} \leq M_{j-1/2}$ is

$$z_j^n + (M_{j-1/2} - z_j^n)\left(\frac{u_{j-1/2}}{u_{j+1/2}} - \frac{\Delta x}{\Delta t}\frac{1}{u_{j+1/2}}\right) \leq \widetilde{z}_{j+1/2}. \tag{22}$$

Finally if we note

$$\begin{cases} a_{j+1/2} = z_j^n + (M_{j-1/2} - z_j^n)\left(\dfrac{u_{j-1/2}}{u_{j+1/2}} - \dfrac{\Delta x}{\Delta t}\dfrac{1}{u_{j+1/2}}\right), \\ A_{j+1/2} = z_j^n + (m_{j-1/2} - z_j^n)\left(\dfrac{u_{j-1/2}}{u_{j+1/2}} - \dfrac{\Delta x}{\Delta t}\dfrac{1}{u_{j+1/2}}\right), \end{cases}$$

then we see that $[a_{j+1/2}, A_{j+1/2}]$ is a trust interval for $\widetilde{z}_{j+1/2}$ that ensures the stability of z in the cell j when $u_{j+1/2} > 0$ and $u_{j-1/2} > 0$ in the sense that

$$\widetilde{z}_{j+1/2} \in [a_{j+1/2}, A_{j+1/2}] \implies z_j^{n+1} \in [m_{j-1/2}, M_{j-1/2}] \implies \text{ stability for } z \text{ in the cell } j.$$

By applying the same lines for the case $u_{j+1/2} < 0$ and $u_{j+3/2} < 0$, we obtain the following proposition.

Proposition 3.1. *Suppose that $\widetilde{z}_{i+1/2}$ belongs to the consistency trust interval $[m_{i-1/2}, M_{i-1/2}]$, for all $i \in \mathbb{Z}$ and that the CFL condition (9) holds. We consider a given $j \in \mathbb{Z}$.*

a) If $u_{j+1/2} > 0$ and $u_{j+3/2} > 0$, we set

$$\begin{cases} a_{j+1/2} = z_j^n + (M_{j-1/2} - z_j^n)\left(\dfrac{u_{j-1/2}}{u_{j+1/2}} - \dfrac{\Delta x}{\Delta t}\dfrac{1}{u_{j+1/2}}\right), \\ A_{j+1/2} = z_j^n + (m_{j-1/2} - z_j^n)\left(\dfrac{u_{j-1/2}}{u_{j+1/2}} - \dfrac{\Delta x}{\Delta t}\dfrac{1}{u_{j+1/2}}\right). \end{cases}$$

We have the following sufficient condition for local stability

$$\widetilde{z}_{j+1/2} \in [a_{j+1/2}, A_{j+1/2}] \implies z_j^{n+1} \in [m_{j-1/2}, M_{j-1/2}] \implies \textit{stability for } z \textit{ in the cell } j.$$

b) If $u_{j+1/2} < 0$ and $u_{j+3/2} < 0$, we set

$$\begin{cases} a_{j+1/2} = z_{j+1}^n + (M_{j+3/2} - z_{j+1}^n)\left(\dfrac{u_{j+3/2}}{u_{j+1/2}} + \dfrac{\Delta x}{\Delta t}\dfrac{1}{u_{j+1/2}}\right), \\ A_{j+1/2} = z_{j+1}^n + (m_{j+3/2} - z_{j+1}^n)\left(\dfrac{u_{j+3/2}}{u_{j+1/2}} + \dfrac{\Delta x}{\Delta t}\dfrac{1}{u_{j+1/2}}\right). \end{cases}$$

Then we have the following sufficient condition for local stability

$$\widetilde{z}_{j+1/2} \in [a_{j+1/2}, A_{j+1/2}] \implies z_{j+1}^{n+1} \in [m_{j+3/2}, M_{j+3/2}] \implies \textit{stability for } z \textit{ in the cell } j+1.$$

The proposition 3.1 defines a trust interval for $\widetilde{z}_{j+1/2}$ that ensures a local stability for z: when $u_{j+1/2} > 0$ and $u_{j-1/2} > 0$, the stability condition deals with the value of z in the cell j, when $u_{j+1/2} < 0$ and $u_{j+3/2} < 0$, it deals with the value of z in the cell $j+1$.

3.3.4. Mass Fraction Stability Constraint for $\widetilde{z}_{j+1/2}$

Recall that according to section 3.1.4 the mass fraction flux is given by $\widetilde{y}_{j+1/2} = \widetilde{z}_{j+1/2}\widetilde{(\rho_1)}_{j+1/2}/\widetilde{\rho}_{j+1/2}$, where $\widetilde{\rho}_{j+1/2} = \widetilde{z}_{j+1/2}\widetilde{(\rho_1)}_{j+1/2} + (1-\widetilde{z}_{j+1/2})\widetilde{(\rho_0)}_{j+1/2}$ and $\widetilde{(\rho_k)}_{j+1/2}$, $k = 0, 1$ are chosen using the upwind value by relation (13). We proceed following similar lines to those in section 3.3.3: when $u_{j+1/2} > 0$ (resp. $u_{j+1/2} < 0$) we consider the neighbouring cell j (resp. $j+1$) whose y value is "emptied" by the flux $y_{j+1/2}$. We consider a special flow pattern when $u_{j-1/2} > 0$ (resp. $u_{j+3/2} < 0$) and a condition on $\widetilde{z}_{j+1/2}$ that guarantees through the definition of $\widetilde{y}_{j+1/2}$ a local maximum principle for y in the cell j (resp. cell $j+1$).

We suppose that $u_{j+1/2} > 0$ and $u_{j-1/2} > 0$ and as in section 3.3.3 for this particular flow configuration we see that we have the following stability condition for the value of y in the cell j

$$\mathfrak{m}_{j-1/2} \leq y_j^{n+1} \leq \mathfrak{M}_{j-1/2} \Longrightarrow \text{ stability for } y \text{ in the cell } j.$$

We seek a sufficient condition that ensures

$$\mathfrak{m}_{j-1/2} \leq y_j^{n+1}. \tag{23}$$

By multiplying (23) by ρ_j^{n+1} and using (10) we see that (23) is equivalent to

$$\mathfrak{m}_{j-1/2}\left[\rho_j^n - \frac{\Delta t}{\Delta x}\left(\widetilde{\rho}_{j+1/2}u_{j+1/2} - \widetilde{\rho}_{j-1/2}u_{j-1/2}\right)\right] \leq \rho_j^n y_j^n - \frac{\Delta t}{\Delta x}\left(\widetilde{\rho}_{j+1/2}\widetilde{y}_{j+1/2}u_{j+1/2} - \widetilde{\rho}_{j-1/2}\widetilde{y}_{j-1/2}u_{j-1/2}\right),$$

which also reads

$$\widetilde{\rho}_{j+1/2}\widetilde{y}_{j+1/2} \leq \frac{\Delta x}{\Delta t}\frac{\rho_j^n}{u_{j+1/2}}\left(y_j^n - \mathfrak{m}_{j-1/2}\right) + \frac{\widetilde{\rho}_{j-1/2}u_{j-1/2}}{u_{j+1/2}}\left(\widetilde{y}_{j-1/2} - \mathfrak{m}_{j-1/2}\right) + \mathfrak{m}_{j-1/2}\widetilde{\rho}_{j+1/2}. \tag{24}$$

As we supposed $\widetilde{z}_{j-1/2} \in [m_{j-1/2}, M_{j-1/2}]$ (see section 3.3.1), therefore $\widetilde{z}_{j-1/2} \in [0,1]$ and then using the assumption (14) we see that $\widetilde{\rho_{j-1/2}} \geq 0$. As we assumed the consistency constraint $\widetilde{y}_{j+1/2} \in [\mathfrak{m}_{j-1/2}, \mathfrak{M}_{j-1/2}]$ to be verified (see section 3.3.2), then we have $\frac{\widetilde{\rho}_{j-1/2}u_{j-1/2}}{u_{j+1/2}}\left(\widetilde{y}_{j-1/2} - \mathfrak{m}_{j-1/2}\right) \geq 0$. Thus we deduce that a sufficient condition for (24) and equivalently (23) to be true is

$$\widetilde{\rho}_{j+1/2}\widetilde{y}_{j+1/2} \leq \frac{\Delta x}{\Delta t}\frac{\rho_j^n}{u_{j+1/2}}\left(y_j^n - \mathfrak{m}_{j-1/2}\right) + \mathfrak{m}_{j-1/2}\widetilde{\rho}_{j+1/2}. \tag{25}$$

The inequality (25) is not an explicit constraint upon $\widetilde{z}_{j+1/2}$ therefore we need to investigate a little further. We use the definition (12) for $\widetilde{\rho}_{j+1/2}\widetilde{y}_{j+1/2}$ and $\widetilde{\rho}_{j+1/2}$ in (25) and as $\widetilde{(\rho_k)}_{j+1/2} = \widetilde{(\rho_k)}_j$, $k = 0, 1$ according to the upwind choice (13) we find that (25) is equivalent to

$$\left\{\widetilde{(\rho_0)}_j\mathfrak{m}_{j-1/2} + \widetilde{(\rho_1)}_j\left(1 - \mathfrak{m}_{j-1/2}\right)\right\}\widetilde{z}_{j+1/2} \leq \frac{\Delta x}{\Delta t}\frac{\rho_j^n}{u_{j+1/2}}\left(y_j^n - \mathfrak{m}_{j-1/2}\right) + \widetilde{(\rho_0)}_j\mathfrak{m}_{j-1/2}. \tag{26}$$

As $\mathfrak{m}_{j-1/2} \in [0,1]$, we see that $\widetilde{(\rho_0)}_j\mathfrak{m}_{j-1/2} + \widetilde{(\rho_1)}_j\left(1 - \mathfrak{m}_{j-1/2}\right) \geq 0$ and therefore that the inequality (26) is indeed an upper bound for $\widetilde{z}_{j+1/2}$. Moreover, we can notice that this bound is explicit as it only involves

terms whose definition does not rely on $\widetilde{z}_{j+1/2}$. For sake of consistency with the formula of proposition 3.1 we propose the following equivalent bound: let us divide the relation (26) by $\widetilde{\rho}_j$ then by noticing

$$\frac{\widetilde{(\rho_k)}}{\widetilde{\rho}_j} = \frac{\widetilde{(y_k)}_j}{\widetilde{(z_k)}_j} = \frac{(y_k)_j^n}{(z_k)_j^n} = \frac{(\rho_k)_j^n}{\rho_j^n}, \quad k = 0, 1,$$

and by using the expression of $\rho_j^n/\widetilde{\rho}_j$ given by (7) we find that (26) reads

$$\widetilde{z}_{j+1/2} \leq z_j^n + \frac{\rho_j^n \left(\mathfrak{m}_{j-1/2} - y_j^n\right)}{(\rho_0)_j^n \mathfrak{m}_{j-1/2} + (\rho_1)_j^n \left(1 - \mathfrak{m}_{j-1/2}\right)} \left(\frac{u_{j-1/2}}{u_{j+1/2}} - \frac{\Delta x}{\Delta t} \frac{1}{u_{j+1/2}}\right).$$

Symmetrically, we can also prove that a sufficient condition for $\widetilde{z}_{j+1/2}$ to be such that $y_j^{n+1} \leq \mathfrak{M}_{j-1/2}$ is provided by

$$z_j^n + \frac{\rho_j^n \left(\mathfrak{M}_{j-1/2} - y_j^n\right)}{(\rho_0)_j^n \mathfrak{M}_{j-1/2} + (\rho_1)_j^n \left(1 - \mathfrak{M}_{j-1/2}\right)} \left(\frac{u_{j-1/2}}{u_{j+1/2}} - \frac{\Delta x}{\Delta t} \frac{1}{u_{j+1/2}}\right) \leq \widetilde{z}_{j+1/2}.$$

Finally if we note

$$\begin{cases} b_{j+1/2} = z_j^n + \dfrac{\rho_j^n \left(\mathfrak{M}_{j-1/2} - y_j^n\right)}{(\rho_0)_j^n \mathfrak{M}_{j-1/2} + (\rho_1)_j^n \left(1 - \mathfrak{M}_{j-1/2}\right)} \left(\dfrac{u_{j-1/2}}{u_{j+1/2}} - \dfrac{\Delta x}{\Delta t} \dfrac{1}{u_{j+1/2}}\right), \\ B_{j+1/2} = z_j^n + \dfrac{\rho_j^n \left(\mathfrak{m}_{j-1/2} - y_j^n\right)}{(\rho_0)_j^n \mathfrak{m}_{j-1/2} + (\rho_1)_j^n \left(1 - \mathfrak{m}_{j-1/2}\right)} \left(\dfrac{u_{j-1/2}}{u_{j+1/2}} - \dfrac{\Delta x}{\Delta t} \dfrac{1}{u_{j+1/2}}\right), \end{cases}$$

we see that $[b_{j+1/2}, B_{j+1/2}]$ is a "trust interval" for choosing $\widetilde{z}_{j+1/2}$ that ensures a local stability for y in the cell j when $u_{j+1/2} > 0$ and $u_{j-1/2} > 0$ in the following sense

$$\widetilde{z}_{j+1/2} \in [b_{j+1/2}, B_{j+1/2}] \implies y_j^{n+1} \in [\mathfrak{m}_{j-1/2}, \mathfrak{M}_{j-1/2}] \implies \text{ stability for } y \text{ in the cell } j.$$

We can perform a similar analysis for the case $u_{j+1/2} < 0$ and $u_{j+3/2} < 0$ and finally we obtain the following proposition.

Proposition 3.2. *Suppose that $\widetilde{z}_{i+1/2} \in [m_{i-1/2}, M_{i-1/2}]$ and suppose that $\widetilde{y}_{i+1/2} \in [\mathfrak{m}_{i-1/2}, \mathfrak{M}_{i-1/2}]$, for all $i \in \mathbb{Z}$ and that the CFL condition (9) holds. Consider a given $j \in \mathbb{Z}$.*

a) If $u_{j+1/2} > 0$ and $u_{j-1/2} > 0$ then we set

$$\begin{cases} b_{j+1/2} = z_j^n + \dfrac{\rho_j^n \left(\mathfrak{M}_{j-1/2} - y_j^n\right)}{(\rho_0)_j^n \mathfrak{M}_{j-1/2} + (\rho_1)_j^n \left(1 - \mathfrak{M}_{j-1/2}\right)} \left(\dfrac{u_{j-1/2}}{u_{j+1/2}} - \dfrac{\Delta x}{\Delta t} \dfrac{1}{u_{j+1/2}}\right), \\ B_{j+1/2} = z_j^n + \dfrac{\rho_j^n \left(\mathfrak{m}_{j-1/2} - y_j^n\right)}{(\rho_0)_j^n \mathfrak{m}_{j-1/2} + (\rho_1)_j^n \left(1 - \mathfrak{m}_{j-1/2}\right)} \left(\dfrac{u_{j-1/2}}{u_{j+1/2}} - \dfrac{\Delta x}{\Delta t} \dfrac{1}{u_{j+1/2}}\right). \end{cases}$$

We have the following sufficient condition for local stability

$$\widetilde{z}_{j+1/2} \in [b_{j+1/2}, B_{j+1/2}] \implies y_j^{n+1} \in [\mathfrak{m}_{j-1/2}, \mathfrak{M}_{j-1/2}] \implies \textit{ stability for } y \textit{ in the cell } j.$$

b) If $u_{j+1/2} < 0$ and $u_{j+3/2} < 0$ then we set

$$\begin{cases} b_{j+1/2} = z_{j+1}^n + \dfrac{\rho_{j+1}^n \left(\mathfrak{M}_{j+3/2} - y_{j+1}^n\right)}{(\rho_0)_{j+1}^n \mathfrak{M}_{j+3/2} + (\rho_1)_{j+1}^n \left(1 - \mathfrak{M}_{j+3/2}\right)} \left(\dfrac{u_{j+3/2}}{u_{j+1/2}} + \dfrac{\Delta x}{\Delta t} \dfrac{1}{u_{j+1/2}}\right), \\ B_{j+1/2} = z_{j+1}^n + \dfrac{\rho_{j+1}^n \left(\mathfrak{m}_{j+3/2} - y_{j+1}^n\right)}{(\rho_0)_{j+1}^n \mathfrak{m}_{j+3/2} + (\rho_1)_{j+1}^n \left(1 - \mathfrak{m}_{j+3/2}\right)} \left(\dfrac{u_{j+3/2}}{u_{j+1/2}} + \dfrac{\Delta x}{\Delta t} \dfrac{1}{u_{j+1/2}}\right). \end{cases}$$

We have the following sufficient condition for local stability

$$\widetilde{z}_{j+1/2} \in [b_{j+1/2}, B_{j+1/2}] \implies y_{j+1}^{n+1} \in [\mathfrak{m}_{j+3/2}, \mathfrak{M}_{j+3/2}] \implies \textit{stability for } y \textit{ in the cell } j+1.$$

3.3.5. Existence of the Trust Interval

In the previous sections we exhibited several "trust intervals" which respectively ensure consistency for the flux $\widetilde{z}_{j+1/2}$ (see section 3.3.1), consistency for the flux $\widetilde{y}_{j+1/2}$ (see section 3.3.2), stability for the variable z (see section 3.3.3) and stability for the variable y (see section 3.3.4). Let us first remark that we did not rule out the fact that some of these intervals may be empty. Moreover, as we wish to impose all of these features we need to consider a trust interval $I_{j+1/2}$ that intersects all of the previously mentioned intervals, namely

$$I_{j+1/2} = [m_{j+1/2}, M_{j+1/2}] \cap [d_{j+1/2}, D_{j+1/2}] \cap [a_{j+1/2}, A_{j+1/2}] \cap [b_{j+1/2}, B_{j+1/2}]. \tag{27}$$

Consequently, we also need to check that $I_{j+1/2} \neq \emptyset$. The answer to both questions lies in the fact that the upwind (relatively to the velocity $u_{j+1/2}$) value for $\widetilde{z}_{j+1/2}$ belongs to all of the previous intervals. Indeed we have the following result.

Proposition 3.3. *Let $j \in \mathbb{Z}$, let us define $I_{j+1/2}$ according to relation* (27).
a) If $u_{j+1/2} > 0$ and $u_{j-1/2} > 0$ then $z_j^n \in I_{j+1/2} \neq \emptyset$.
b) If $u_{j+1/2} < 0$ and $u_{j+3/2} < 0$ then $z_{j+1}^n \in I_{j+1/2} \neq \emptyset$.

Proof. Let us suppose $u_{j+1/2} > 0$ and $u_{j-1/2} > 0$. In this case we need to show that

$$\widetilde{z}_j = z_j^n \in [m_{j+1/2}, M_{j+1/2}] \cap [d_{j+1/2}, D_{j+1/2}] \cap [a_{j+1/2}, A_{j+1/2}] \cap [b_{j+1/2}, B_{j+1/2}].$$

First we see that

$$m_{j+1/2} = \min(z_j^n, z_{j+1}^n,) \leq z_j^n.$$

Let us turn to the consistency of the flux $\widetilde{y}_{j+1/2}$. The upwind choice (13) provides in our case that

$$\widetilde{(\rho_1)}_{j+1/2} = \widetilde{(\rho_1)}_j = \widetilde{\rho}_j \frac{\widetilde{y}_j}{\widetilde{z}_j} = \widetilde{\rho}_j \frac{y_j^n}{z_j^n} \quad \text{and} \quad \widetilde{(\rho_0)}_{j+1/2} = \widetilde{(\rho_0)}_j = \widetilde{\rho}_j \frac{1-\widetilde{y}_j}{1-\widetilde{z}_j} = \widetilde{\rho}_j \frac{1-y_j^n}{1-z_j^n}.$$

Then according to the definition (17) we have

$$d_{j+1/2} = \frac{\mathfrak{m}_{j+1/2} \frac{1-y_j^n}{1-z_j^n}}{(1-\mathfrak{m}_{j+1/2}) \frac{y_j^n}{z_j^n} + \mathfrak{m}_{j+1/2} \frac{1-y_j^n}{1-z_j^n}}.$$

Therefore

$$d_{j+1/2} - z_j^n = -\frac{z_j^n (1-z_j^n)(y_j^n - \mathfrak{m}_{j+1/2})}{(1-\mathfrak{m}_{j+1/2}) y_j^n (1-z_j^n) + \mathfrak{m}_{j+1/2}(1-y_j^n) z_j^n}.$$

As $\mathfrak{m}_{j+1/2}$, z_j^n and y_j^n all belong to $[0,1]$ and as by definition $\mathfrak{m}_{j+1/2} = \min(y_j^n, y_{j+1}^n) \leq y_j^n$, we deduce that

$$d_{j+1/2} \leq z_j^n.$$

With the definitions in proposition 3.1

$$a_{j+1/2} = z_j^n - \frac{(M_{j-1/2} - z_j^n)}{u_{j+1/2}} \frac{\Delta x}{\Delta t} \left(1 - \frac{\Delta t}{\Delta x} u_{j-1/2}\right).$$

As by definition $M_{j-1/2} = \max(z_{j-1}^n, z_j^n) \leq z_j^n$ and as the CFL condition (9) imposes that $u_{j-1/2}\frac{\Delta t}{\Delta x} \leq 1$, we deduce that

$$a_{j+1/2} \leq z_j^n.$$

For the constraint of stability for the variable y, according to the definitions given in proposition 3.2

$$b_{j+1/2} = z_j^n - \frac{\rho_j^n \frac{\Delta x}{\Delta t}\frac{\mathfrak{M}_{j-1/2}-y_j^n}{u_{j+1/2}}}{(\rho_0)_j^n \mathfrak{M}_{j-1/2} + (\rho_1)_j^n(1-\mathfrak{M}_{j-1/2})}\left(1 - \frac{\Delta t}{\Delta x}u_{j-1/2}\right).$$

We know that $\mathfrak{M}_{j-1/2} = \max(y_{j-1}^n, y_j^n) \geq y_j^n$ and that $\mathfrak{M}_{j-1/2} \in [0,1]$, altogether with the positivity hypothesis (14) and the CFL condition (9), we obtain that

$$b_{j+1/2} \leq z_j^n.$$

Using similar lines we also obtain that $z_j^n \leq M_{j+1/2}$, $z_j^n \leq D_{j+1/2}$, $z_j^n \leq A_{j+1/2}$ and $z_j^n \leq B_{j+1/2}$, which proves the point a).

The point b) can be stated using the same arguments. □

3.4. Overall Algorithm

Let us first verify that the anti-diffusive numerical scheme is conservative relatively to the variables ρy, ρ, ρu and ρe. Indeed, using the relations (7) and (10) we see that the overall numerical scheme reads

$$\begin{cases} \dfrac{\rho_j^{n+1}y_j^{n+1} - \rho_j^n y_j^n}{\Delta t} + \dfrac{1}{\Delta x}\Big(\widetilde{\rho}_{j+1/2}\widetilde{y}_{j+1/2}u_{j+1/2} - \widetilde{\rho}_{j-1/2}\widetilde{y}_{j-1/2}u_{j-1/2}\Big) = 0, \\ \dfrac{\rho_j^{n+1} - \rho_j^n}{\Delta t} + \dfrac{1}{\Delta x}\Big(\widetilde{\rho}_{j+1/2}u_{j+1/2} - \widetilde{\rho}_{j-1/2}u_{j-1/2}\Big) = 0, \\ \dfrac{\rho_j^{n+1}u_j^{n+1} - \rho_j^n u_j^n}{\Delta t} + \dfrac{1}{\Delta x}\Big(\widetilde{\rho}_{j+1/2}\widetilde{u}_{j+1/2}u_{j+1/2} + P_{j+1/2} - \widetilde{\rho}_{j-1/2}\widetilde{u}_{j-1/2}u_{j-1/2} - P_{j-1/2}\Big) = 0, \\ \dfrac{\rho_j^{n+1}e_j^{n+1} - \rho_j^n e_j^n}{\Delta t} + \dfrac{1}{\Delta x}\Big(\widetilde{\rho}_{j+1/2}\widetilde{e}_{j+1/2}u_{j+1/2} + P_{j+1/2}u_{j+1/2} - \widetilde{\rho}_{j-1/2}\widetilde{e}_{j-1/2}u_{j-1/2} - P_{j-1/2}u_{j-1/2}\Big) = 0, \\ \dfrac{z_j^{n+1} - z_j^n}{\Delta t} + \dfrac{1}{\Delta x}\Big(\widetilde{z}_{j+1/2}u_{j+1/2} - \widetilde{z}_{j-1/2}u_{j-1/2}\Big) - \dfrac{1}{\Delta x}z_j^n\Big(u_{j+1/2} - u_{j-1/2}\Big) = 0. \end{cases}$$

The scheme consists in a conservative part for $\rho\mathbf{V} = [\rho y, \rho, \rho u, \rho e]^T$ and advection-type discretization for z which shows that our algorithm is quasi-conservative as the algorithm presented in [2, 3].

We now give a step-by-step view of the full anti-diffusive algorithm.

1. For each cell interface $j+1/2$, compute $u_{j+1/2}$, $(\rho c)_{j+1/2}$ and $P_{j+1/2}$.
2. Compute Δt in agreement with the CFL constraint (9).
3. Compute the state $(\widetilde{\rho}\widetilde{\mathbf{V}}, \widetilde{z})_j$ according to (7) for all j.
4. For each cell interface $j+1/2$, compute the numerical flux $\widetilde{z}_{j+1/2}$ as follows:
   - if $u_{j+1/2} > 0$
     - if $u_{j-1/2} > 0$, compute the bounds of the trust interval $I_{j+1/2} = [\omega_{j+1/2}, \Omega_{j+1/2}]$ defined by (27), then

$$\begin{cases} \text{if } z_{j+1}^n \leq \omega_{j+1/2}, & \text{then choose } \widetilde{z}_{j+1/2} = \omega_{j+1/2}, \\ \text{if } \omega_{j+1/2} < z_{j+1}^n < \Omega_{j+1/2}, & \text{then choose } \widetilde{z}_{j+1/2} = z_{j+1}^n, \\ \text{if } \Omega_{j+1/2} \leq z_{j+1}^n, & \text{then choose } \widetilde{z}_{j+1/2} = \Omega_{j+1/2}. \end{cases}$$

– if $u_{j-1/2} < 0$, we choose the upwind value

$$\widetilde{z}_{j+1/2} = z_j^n.$$

- if $u_{j+1/2} < 0$
  - if $u_{j+3/2} > 0$, we choose the upwind value

$$\widetilde{z}_{j+1/2} = z_{j+1}^n.$$

  - if $u_{j+3/2} < 0$, compute the bounds of the trust interval $I_{j+1/2} = [\omega_{j+1/2}, \Omega_{j+1/2}]$ defined by (27), then

$$\begin{cases} \text{if } z_j^n \le \omega_{j+1/2}, & \text{then choose } \widetilde{z}_{j+1/2} = \omega_{j+1/2}, \\ \text{if } \omega_{j+1/2} < z_j^n < \Omega_{j+1/2}, & \text{then choose } \widetilde{z}_{j+1/2} = z_j^n, \\ \text{if } \Omega_{j+1/2} \le z_{j+1}^n, & \text{then choose } \widetilde{z}_{j+1/2} = \Omega_{j+1/2}. \end{cases}$$

5. For each cell interface $j+1/2$, compute the interface values $\widetilde{y}_{j+1/2}$, $\widetilde{\rho}_{j+1/2}$, $\widetilde{\rho\varepsilon}_{j+1/2}$ and $\widetilde{u}_{j+1/2}$, according to (12) and (13).
6. Update $(\widetilde{\rho}\widetilde{\mathbf{V}}, \widetilde{z})_j$ into $(\rho\mathbf{V}, z)_j^{n+1}$ using (10) for all j.

4. Evolution of Constant Pressure and Velocity Profiles

A classical issue for the simulation of compressible flows with two-phase interfaces lies in ensuring that the numerical scheme will not developp spurious oscillations at the material interface. Indeed, although the pressure and the velocity are Riemann invariants for the contact discontinuity associated with the material interface of the five-equation model [2, 3], when the interface is smeared by the discretization, inconsistencies may appear between the extended EOS, the state variable $(\rho\mathbf{V}, z)$ and the pressure P. This question has been examined by several authors for the past years within the framework of various two-phase interface models [11, 12, 1, 25, 22, 21, 26, 2, 27, 14, 3, 42, 15, 7].

For the five-equation model with isobaric closure, the Roe-type scheme [20] presented in [2, 3] provides a good discretization of the Riemann invariants across the material interface in the sense that it preserves some constant pressure and velocity profiles for a wide range of EOSs. The proposition 4.1 shows that the anti-diffusive scheme is endowed with a similar property.

Proposition 4.1. *Let $(\rho^n\mathbf{V}^n, z^n)$ be the approximated state variable at instant $t^n = n\Delta t$ computed by the anti-diffusive scheme. Suppose that $(\rho^n\mathbf{V}^n, z^n)$ is a contact discontinuity with uniform velocity and pressure such that for all $j \in \mathbb{Z}$ we have*

$$P_j^n = \overline{P}, \qquad u_j^n = \overline{u}, \tag{28}$$

$$(\rho_0)_j^n = \overline{\rho_0}, \qquad (\rho_1)_j^n = \overline{\rho_1}, \tag{29}$$

where $\overline{P}$, $\overline{u}$, $\overline{\rho_0}$, $\overline{\rho_1}$ are constants. Then, the approximated state variable $(\rho^{n+1}\mathbf{V}^{n+1}, z^{n+1})$ computed by the anti-diffusive scheme verifies

$$P_j^{n+1} = \overline{P}, \qquad u_j^{n+1} = \overline{u}, \qquad \forall j \in \mathbb{Z} \tag{30}$$

$$(\rho_0)_j^{n+1} = \overline{\rho_0}, \qquad (\rho_1)_j^{n+1} = \overline{\rho_1}, \qquad \forall j \in \mathbb{Z}. \tag{31}$$

Proof. We use thereafter the same notations as in section 3. We suppose here without loss of generality that $\overline{u} > 0$. Before going any further, let us remark that as the pressure and both phasic densities are uniform at time t^n, then both phasic internal energies at time t^n are also uniform. Indeed, using the pure fluids state law $(\rho_k, P_k) \mapsto \rho_k\varepsilon_k(\rho_k, P_k)$, one can set

$$\forall j \in \mathbb{Z}, \quad (\rho_k\varepsilon_k)_j^n = (\rho_k\varepsilon_k)(\overline{\rho_k}, \overline{P}) = \overline{\rho_k\varepsilon_k}.$$

Let us examine the Lagrangian approximated solution obtained by the Lagrange step (7). As pressure and velocity are uniform, the fluxes for the Lagrange step defined by relations (8) read

$$u_{j+1/2} = \overline{u}, \qquad P_{j+1/2} = \overline{P}, \qquad \forall j \in \mathbb{Z}.$$

After the Lagrange step defined by relations (7)-(8) we obtain for all $j \in \mathbb{Z}$

$$\widetilde{z}_j = z_j^n, \qquad \widetilde{y}_j = y_j^n, \qquad \widetilde{\tau}_j = \tau_j^n, \qquad \widetilde{u}_j = u_j^n = \overline{u}, \qquad \widetilde{e}_j = e_j^n.$$

First we deduce that

$$\widetilde{(\rho_k)}_j = \frac{\widetilde{(y_k)}_j}{\widetilde{\tau}_j\widetilde{(z_k)}_j} = \frac{(y_k)_j^n}{\tau_j^n(z_k)_j^n} = (\rho_k)_j^n = \overline{\rho_k}, \quad k = 0, 1.$$

We also have $\widetilde{\varepsilon}_j = \varepsilon_j^n$ and thus $\widetilde{(\rho\varepsilon)}_j = (\rho\varepsilon)_j^n$. The pressure $\widetilde{P}_j$ and the phasic energies $\widetilde{(\rho_k\varepsilon_k)}_j$, $k = 0, 1$ associated with the updated Lagrangian state $(\widetilde{\rho_j\mathbf{V}}_j, \widetilde{z}_j)$ verify relations (2), which reads here

$$\begin{cases} \widetilde{P}_j = P_0\big[\overline{\rho_0}, \widetilde{(\rho_0\varepsilon_0)}_j\big] = P_1\big[\overline{\rho_1}, \widetilde{(\rho_1\varepsilon_1)}_j\big], \\ \widetilde{(\rho\varepsilon)}_j = (\rho\varepsilon)_j^n = z_j^n\widetilde{(\rho_1\varepsilon_1)}_j + (1 - z_j^n)\widetilde{(\rho_0\varepsilon_0)}_j. \end{cases} \tag{32}$$

However, we know that the pressure $P_j^n = \overline{P}$ and the phasic energies $(\rho_k\varepsilon_k)_j^n = \overline{\rho_k\varepsilon_k}$, $k = 0, 1$ associated with the state variable $(\rho_j^n\mathbf{V}_j^n, z_j^n)$ at time t^n verify relations (2), namely

$$\begin{cases} \overline{P} = P_0\big[\overline{\rho_0}, \overline{\rho_0\varepsilon_0}\big] = P_1\big[\overline{\rho_1}, \overline{\rho_1\varepsilon_1}\big], \\ (\rho\varepsilon)_j^n = z_j^n\overline{\rho_1\varepsilon_1} + (1 - z_j^n)\overline{\rho_0\varepsilon_0}. \end{cases} \tag{33}$$

We see then that $(\widetilde{P}_j, \widetilde{(\rho_0\varepsilon_0)}_j, \widetilde{(\rho_1\varepsilon_1)}_j)$ and $(\overline{P}, \overline{\rho_0\varepsilon_0}, \overline{\rho_1\varepsilon_1})$ are respectively solution of (32) and (33), which are the same system. According to the hypotheses of section 2, the isobaric closure system (2) admits a single solution. Therefore

$$\widetilde{P}_j = \overline{P}, \qquad \widetilde{(\rho_0\varepsilon_0)}_j = \overline{\rho_0\varepsilon_0}, \qquad \widetilde{(\rho_1\varepsilon_1)}_j = \overline{\rho_1\varepsilon_1}, \qquad \forall j \in \mathbb{Z}.$$

We shall now consider the Remap step (10). In our case we have

$$\rho_j^{n+1} - \rho_j^n + \frac{\Delta t}{\Delta x}\overline{u}\left(\widetilde{\rho}_{j+1/2} - \widetilde{\rho}_{j-1/2}\right) = 0, \tag{34}$$

$$\rho_j^{n+1}y_j^{n+1} - \rho_j^n y_j^n + \frac{\Delta t}{\Delta x}\overline{u}\left(\widetilde{\rho}_{j+1/2}\widetilde{y}_{j+1/2} - \widetilde{\rho}_{j-1/2}\widetilde{y}_{j-1/2}\right) = 0, \tag{35}$$

$$\rho_j^{n+1}u_j^{n+1} - \rho_j^n\overline{u} + \frac{\Delta t}{\Delta x}\overline{u}\left(\widetilde{\rho}_{j+1/2}\widetilde{u}_{j+1/2} - \widetilde{\rho}_{j-1/2}\widetilde{u}_{j-1/2}\right) = 0, \tag{36}$$

$$\rho_j^{n+1}e_j^{n+1} - \rho_j^n\widetilde{e}_j + \frac{\Delta t}{\Delta x}\overline{u}\left(\widetilde{\rho}_{j+1/2}\widetilde{e}_{j+1/2} - \widetilde{\rho}_{j-1/2}\widetilde{e}_{j-1/2}\right) = 0, \tag{37}$$

$$z_j^{n+1} - z_j^n + \frac{\Delta t}{\Delta x}\overline{u}(\widetilde{z}_{j+1/2} - \widetilde{z}_{j-1/2}) = 0. \tag{38}$$

As we supposed $\overline{u} > 0$, the upwind cell relatively to the interface $j+1/2$ is the cell j. Therefore, we have for all $j \in \mathbb{Z}$

$$\begin{aligned} \widetilde{(\rho_1)}_{j+1/2} &= \widetilde{(\rho_1)}_j = \overline{\rho_1}, & \widetilde{(\rho_2)}_{j+1/2} &= \widetilde{(\rho_2)}_j = \overline{\rho_2}, \\ \widetilde{(\rho_1\varepsilon_1)}_{j+1/2} &= \widetilde{(\rho_1\varepsilon_1)}_j = \overline{\rho_1\varepsilon_1}, & \widetilde{(\rho_2\varepsilon_2)}_{j+1/2} &= \widetilde{(\rho_2\varepsilon_2)}_j = \overline{\rho_2\varepsilon_2}, \\ \widetilde{u}_{j+1/2} &= \widetilde{u}_j = \overline{u}. \end{aligned}$$

Then, injecting relation (34) into (36) provides that $\rho_j^{n+1}(u_j^{n+1} - \overline{u}) = 0$. If we suppose that there is no vacuum formation, namely $\rho_j^{n+1} > 0$ for all $j \in \mathbb{Z}$, we obtain

$$u_j^{n+1} = \overline{u}, \quad \forall j \in \mathbb{Z}.$$

As a consequence, all the terms related to the kinetic energy vanish in relation (37), which gives

$$\begin{aligned} \rho_j^{n+1}\varepsilon_j^{n+1} &= \rho_j^n\widetilde{\varepsilon}_j - \frac{\Delta t}{\Delta x}\left(\widetilde{\rho}_{j+1/2}\widetilde{\varepsilon}_{j+1/2} - \widetilde{\rho}_{j-1/2}\widetilde{\varepsilon}_{j-1/2}\right) = \rho_j^n\widetilde{\varepsilon}_j - \frac{\Delta t}{\Delta x}\left(\widetilde{\rho}_{j+1/2}\widetilde{e}_{j+1/2} - \widetilde{\rho}_{j-1/2}\widetilde{e}_{j-1/2}\right) \\ &= \sum_{k=0,1}(z_k)_j^n\overline{\rho_k\varepsilon_k} - \frac{\Delta t}{\Delta x}\left(\sum_{k=0,1}\widetilde{(z_k)}_{j+1/2}\overline{\rho_k\varepsilon_k} - \sum_{k=0,1}\widetilde{(z_k)}_{j-1/2}\overline{\rho_k\varepsilon_k}\right) \\ &= \sum_{k=0,1}\overline{\rho_k\varepsilon_k}\left((z_k)_j^n - \frac{\Delta t}{\Delta x}\overline{u} - [\widetilde{(z_k)}_{j+1/2} - \widetilde{(z_k)}_{j-1/2}]\right). \end{aligned}$$

Thanks to relation (38) we obtain

$$\rho_j^{n+1}\varepsilon_j^{n+1} = z_j^{n+1}\overline{\rho_1\varepsilon_1} + (1 - z_j^{n+1})\overline{\rho_0\varepsilon_0}. \tag{39}$$

By considering the mass fraction remap provided by relation (35) and the fluxes definition (12) we find that

$$z_j^{n+1}(\rho_1)_j^{n+1} - z_j^n\overline{\rho_1} + \frac{\Delta t}{\Delta x}\overline{u\rho_1}\left[\widetilde{z}_{j+1/2} - \widetilde{z}_{j-1/2}\right].$$

Therefore, we have $z_j^{n+1}[(\rho_1)_j^{n+1} - \overline{\rho_1}] = 0$, which implies that for all $j \in \mathbb{Z}$

$$(\rho_1)_j^{n+1} = \overline{\rho_1} \quad \text{and similarly} \quad (\rho_0)_j^{n+1} = \overline{\rho_0}.$$

The pressure P_j^{n+1} is thus solution of the system

$$\begin{cases} P_1\left(\overline{\rho_1}, (\rho_1\varepsilon_1)_j^{n+1}\right) = P_0\left(\overline{\rho_0}, (\rho_0\varepsilon_0)_j^{n+1}\right), \\ (\rho\varepsilon)_j^{n+1} = z_j^{n+1}(\rho_1\varepsilon_1)_j^{n+1} + (1 - z_j^{n+1})(\rho_0\varepsilon_0)_j^{n+1}. \end{cases} \tag{40}$$

However, thanks to relation (39) we can see that a possible solution for (40) reads

$$(\rho_1\varepsilon_1)_j^{n+1} = \overline{\rho_1\varepsilon_1}, \quad (\rho_1\varepsilon_0)_j^{n+1} = \overline{\rho_0\varepsilon_0}, \quad P_j^{n+1} = P_1\left(\overline{\rho_1}, \overline{\rho_1\varepsilon_1}\right) = P_0\left(\overline{\rho_0}, \overline{\rho_0\varepsilon_0}\right) = \overline{P}.$$

According to the hypotheses of section 2 regarding the isobaric closure system, we know that this solution is unique and finally, we can conclude that $P_j^{n+1} = \overline{P}$. □

Remark 3. *Let us underline that the proof of proposition 4.1 does not depend on the anti-diffusive aspect of the numerical scheme.*

In section 5 we shall present 1D and 2D numerical results of pure interface advection for fluids with complex or analytical EOSs that concur with the proposition 4.1.

5. Numerical Results

We present a selection of numerical tests performed with the anti-diffusive scheme and the classical upwind Lagrange-Remap solver for the five-equation model with isobaric closure. For both schemes, the two-dimensional tests have been achieved thanks to a simple directional splitting. Let us remark that our study is limited to the comparison of the anti-diffusive scheme against the upwind scheme for the following reasons: first, we believe that both schemes perform in a very similar way far from the interface. Numerical tests will help to shed some light on this matter. Second, there is a very broad range of numerical schemes and interface capture techniques, like Level Set techniques Front Tracking or VOF methods, that would be worth comparing to the anti-diffusive scheme. Achieving such an exhaustive comparison would be very lengthy and is beyond the scope of the present work.

5.1. 1D Advection Test

The first test is a 1D interface advection between two materials: the first fluid (denoted by fluid 0) is governed by a tabulated EOS and the second fluid (denoted by fluid 1) is a stiffened gas. For the sake of simplicity and ease of reproducibility we tabulated the following van der Waals gas

$$P = \left(\frac{\gamma_0 - 1}{1 - b_0\rho}\right)(\rho\varepsilon + a_0\rho^2) - a_0\rho^2, \quad \gamma_0 = 1.4, \quad b_0 = 10^{-3}, \quad a_0 = 5.$$

The table data were obtained by discretizing the (ρ, P) plane limited by $0 \leq \rho \leq 990$ and $10^4 \leq P \leq 10^9$ over an uniform grid of 1000×1000 nodes. The table provides the values of $\rho\varepsilon$ for each node (ρ, P) and the whole $(\rho, P) \mapsto \rho\varepsilon$ function is given by a Q_1 interpolation. For the tabulated gas, the function $(\rho, \varepsilon) \mapsto P$ is defined implicitly and evaluated by means of a Newton method. The fluid 1 is a stiffened gas whose EOS is given by the following analytical relation

$$P = (\gamma_1 - 1)\rho\varepsilon - \gamma_1\pi_1, \quad \gamma_1 = 4.4, \quad \pi_1 = 6 \times 10^8\,\mathrm{Pa}$$

The pressure of the five-equation model with isobaric closure is then retrieved by solving the equation $P_0 = P_1$ with respect to the variable $\rho_1\varepsilon_1$ with a dichotomy algorithm.

We consider a 1 m long one-dimensional domain with periodic boundary conditions. At $t = 0$, the region $0.3 \leq x \leq 0.7$ corresponds to a 1D bubble of fluid 1 surrounded by the tabulated fluid 0 for $0 \leq x < 0.3$ and $0.7 < x \leq 1$. In the stiffened gas, the initial density is $\rho = 1000\,\mathrm{kg \cdot m^{-3}}$ while in the tabulated fluid it is set to $\rho = 50\,\mathrm{kg \cdot m^{-3}}$. Both velocity u and pressure P are initially uniform in the domain and are set respectively to $u = 1000\,\mathrm{m \cdot s^{-1}}$ and $P = 10^5\,\mathrm{Pa}$. The domain is discretized over a 100 cells mesh and the tests has been performed with the CFL coefficient $C_{\mathrm{CFL}} = 0.99$.

Figures 3, 4 and 6 displays the results obtained with both the anti-diffusive solver the upwind solver. One can see in figure 3 that the color function z remains very sharp throughout the computation with the anti-diffusive solver. At time $t = 3.0\,\mathrm{s}$ after 1 524 000 time steps, the initial pulse shape of the variable is

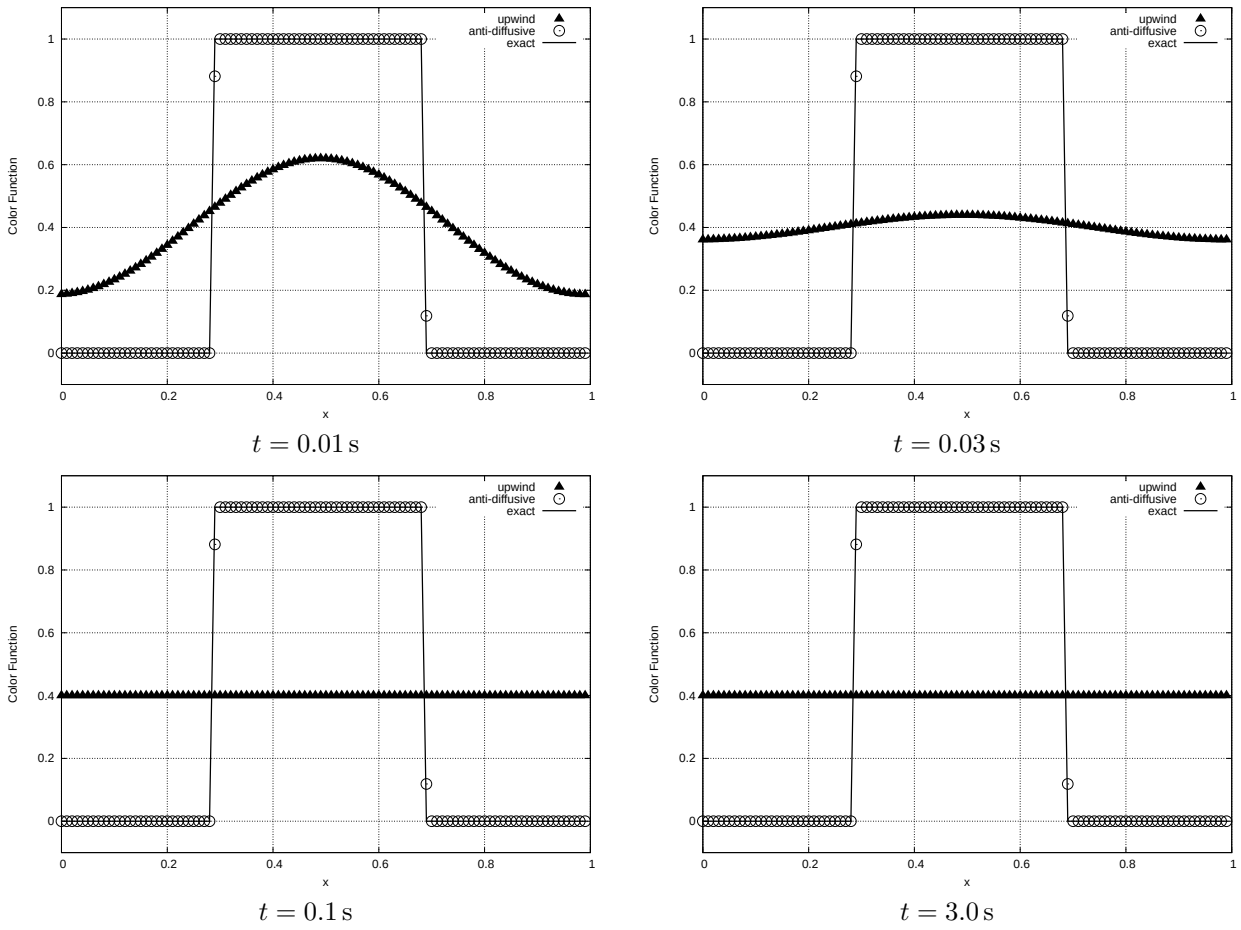

Figure 3: 1D Advection Test. Profiles of the color function obtained with the upwind scheme, the anti-diffusive scheme and the exact solution at instant $t \in \{0.01, 0.03, 0.1, 3.0\}\,\mathrm{s}$

preserved by the anti-diffusive scheme with only two cells affected by the numerical diffusion. Moreover, the position of the approximated pulse shows a very strong match with the exact solution. At the same physical instant the solution computed by the upwind scheme has totally converged to the average value $0.4 = \int_0^1 z(t=0,x)\mathrm{d}x$.

Figure 4 displays the pressure and the velocity at instant $t = 3.0\,\mathrm{s}$ for both upwind and anti-diffusive scheme. One can see that the computed pressure and velocity are left unchanged by both schemes, which demonstrates the ability of the anti-diffusive scheme to preserve the iso-presure and iso-velocity solutions, even in the case of complex and non-analytic EOSs.

While the scheme was not initially designed for such purpose, one can notice in figure 5 that the density variable ρ and the mass fraction variable y both inherit the anti-diffusive property built for the variable z. Indeed, at $t = 3.0\,\mathrm{s}$, the pulse shape of both density and mass fraction is captured with no more than 2 cells of numerical diffusion, while the upwind computed solution is totally diffused.

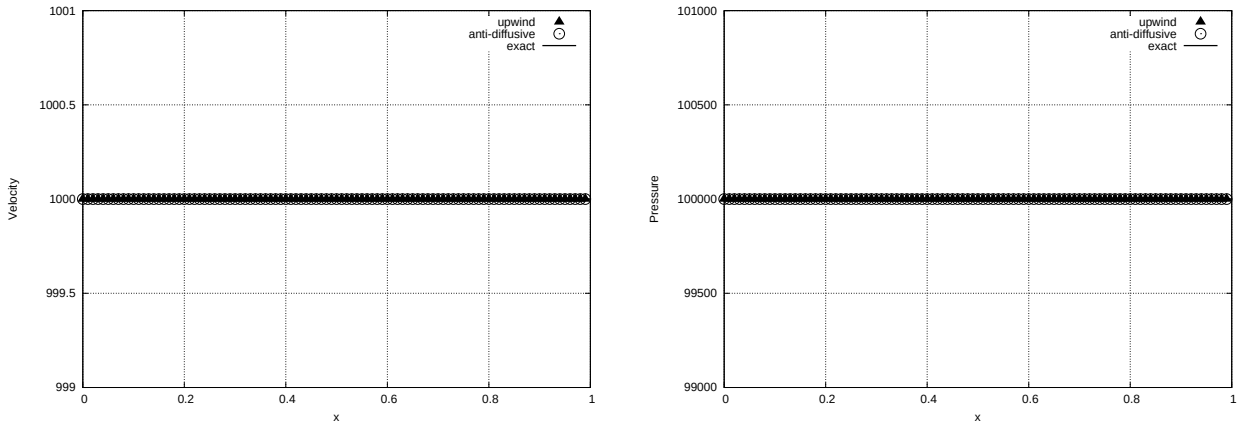

Figure 4: 1D Advection Test. Profiles of the velocity, the pressure obtained with the upwind scheme, the anti-diffusive scheme and the exact solution, at instant $t = 3.0\,\mathrm{s}$.

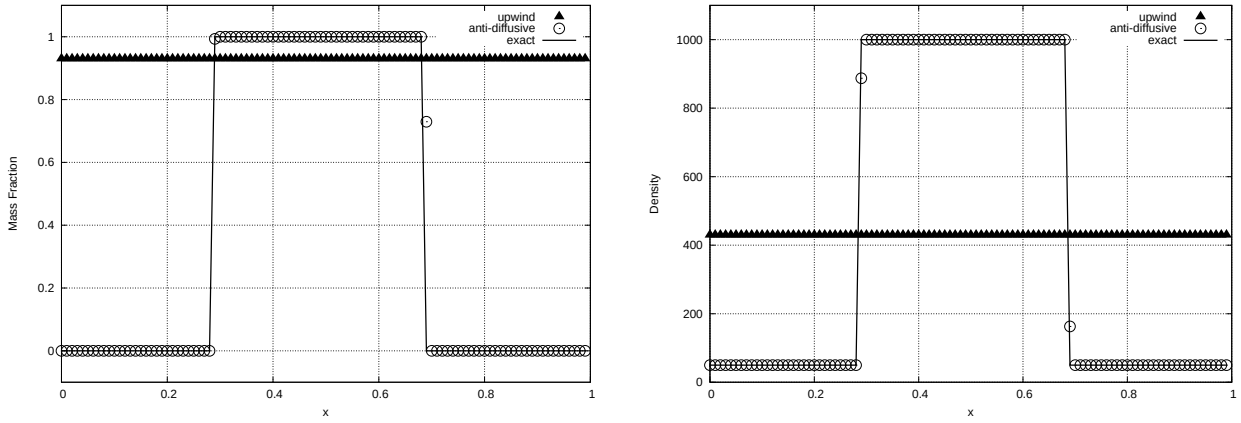

Figure 5: 1D Advection Test. Profiles of the mass fraction y and the density obtained with the upwind scheme, the anti-diffusive scheme and the exact solution, at instant $t = 3.0\,\mathrm{s}$.

The evolution of the numerical diffusion for the color function variable z throughout the computation is given in figure 6 thanks to the graph of the function $N \mapsto \text{percent}(N)$, where N is the number of time steps and $\text{percent}(N)$ is the percent of cells where the variable z is numerically diffused. At an instant $t = t_n$, a cell i is counted as a cell with diffused value of z if $\nu < z_i^n < 1 - \nu$, $\nu = 10^{-6}$. This graph shows that the number of diffusion cells reaches the asymptotic value of $2\,\%$ (2 diffusion cells) after the first time step for the anti-diffusive scheme. On the contrary, the number of diffusion cells for the upwind scheme, grows – as expected – until it reaches $100\,\%$ for $N \simeq 200$.

5.2. Shock Tube Test

We now test the anti-diffusive with a shock tube simulation that is derived from a classical test elaborated by Sod [40]. Our test involves two perfect gases whose EOSs read

$$P_k = (\gamma_k - 1)\rho_k \varepsilon_k, \tag{41}$$

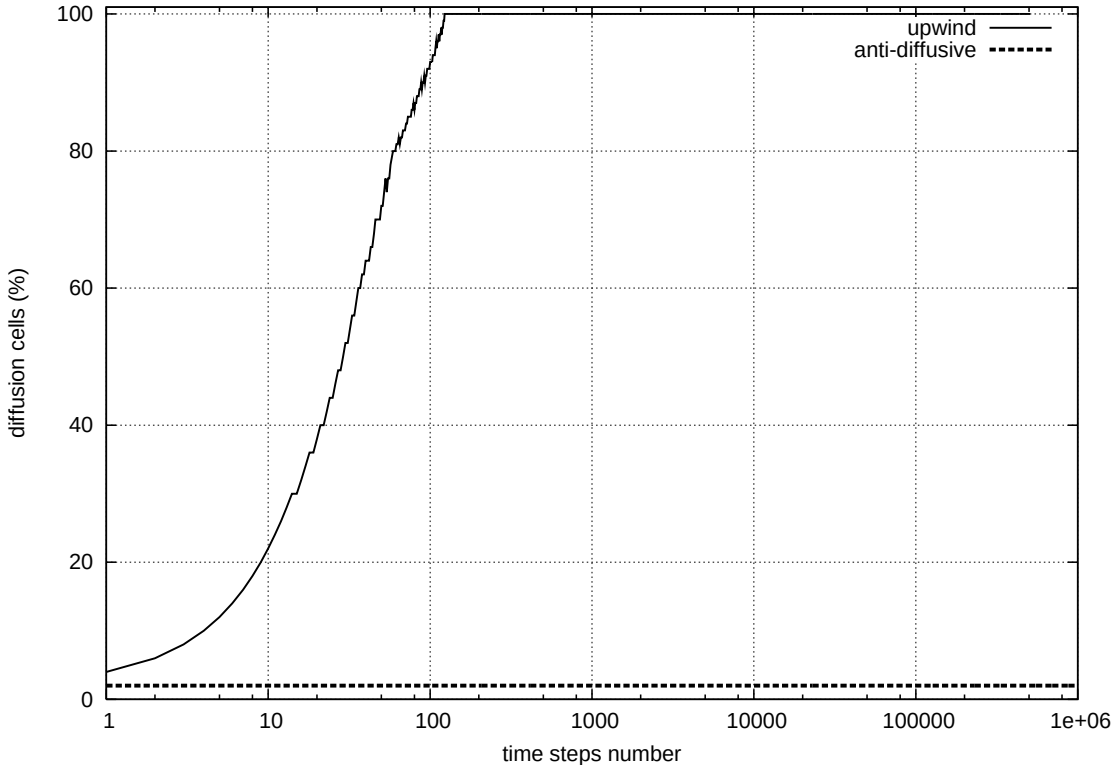

Figure 6: 1D Advection Test. Percent of cells in the domain where the color function z is numerically diffused versus the number of time steps (in log scale), for both the upwind and the anti-diffusive scheme.

and in this case, the parameter $\xi_k = 1/(\gamma_k - 1)$ is a constant.

Both fluids are initially at rest in a 1 m long one-dimensional domain, separated by an interface located at $x = 0.5\,\mathrm{m}$. On each side of the interface, the fluid state at $t = 0$ are is by

$$(\gamma, \rho, u, P) = (1.4, 1.0, 0.0, 1.0), \qquad \text{for } 0.5 > x,$$
$$(\gamma, \rho, u, P) = (2.4, 0.125, 0.0, 0.1), \qquad \text{for } 0.5 < x.$$

The domain is discretized over a 300 cells mesh and both boundary conditions are computed by maintaining constant states. Figure 7 displays the results of the simulation at $t = 0.14\,\mathrm{s}$. By observing the pressure, the velocity and the density variables, one can see that the solution computed by the anti-diffusive scheme shows quite a good agreement with the results of the upwind scheme for the rarefaction wave and the shock wave. The interface is resolved with one or two diffusion cells by the anti-diffusive scheme on the color function z. Whereas the scheme was not designed for this purpose, the diffusion of the mass fraction variable y is also contained. The same phenomenon occurs at the contact discontinuity for the density variable, which is resolved within 2 or 3 cells. Far from the interface, the density profiles computed by both schemes coincide.

Altogether, the above observations suggest that the anti-diffusive mechanism of the anti-diffusive scheme is only triggered at the contact discontinuity. For both the other waves, the shock and the rarefaction, the anti-diffusive scheme simply degenerates to the upwind scheme. This explains the similarities between both set of results. This statement is also consistent with the strong match between the pressure and the velocity computed by both schemes. Indeed these variables are not sensitive to the strength of the contact discontinuity. We shall elaborate further on similar matters in sections 5.3 and 5.5.

We can see that a slight undershoot occurs at the contact discontinuity for the density variable. In order to check that this undershoot is not a sign of rising instability, we performed the same test with a 50 000 cells refined mesh. The results are displayed in figure 9: one can observe that the undershoot has vanished as the space step has decreased. Moreover all the variables ρ, y, z, u, P seem to converge to the exact solution.

The amount of diffusion cells for the color function has been measured with both upwind and anti-diffusive schemes. The results are displayed in figure 8. The behaviour of the anti-diffusive scheme is quite coherent with the previous results for the 1D advection test in section 5.1: straight after the very first time steps, the shock departs from its original position. The interface that was originally coincident with the shock becomes purely advected by the local velocity that becomes constant in the vicinity of the contact discontinuity. Then, the number of diffusion cells for the upwind scheme keeps growing as the number of time steps increases, while for the anti-diffusive scheme the percentage of diffusion cells seems to reach instantaneously an asymptotic value of 0.33 %.

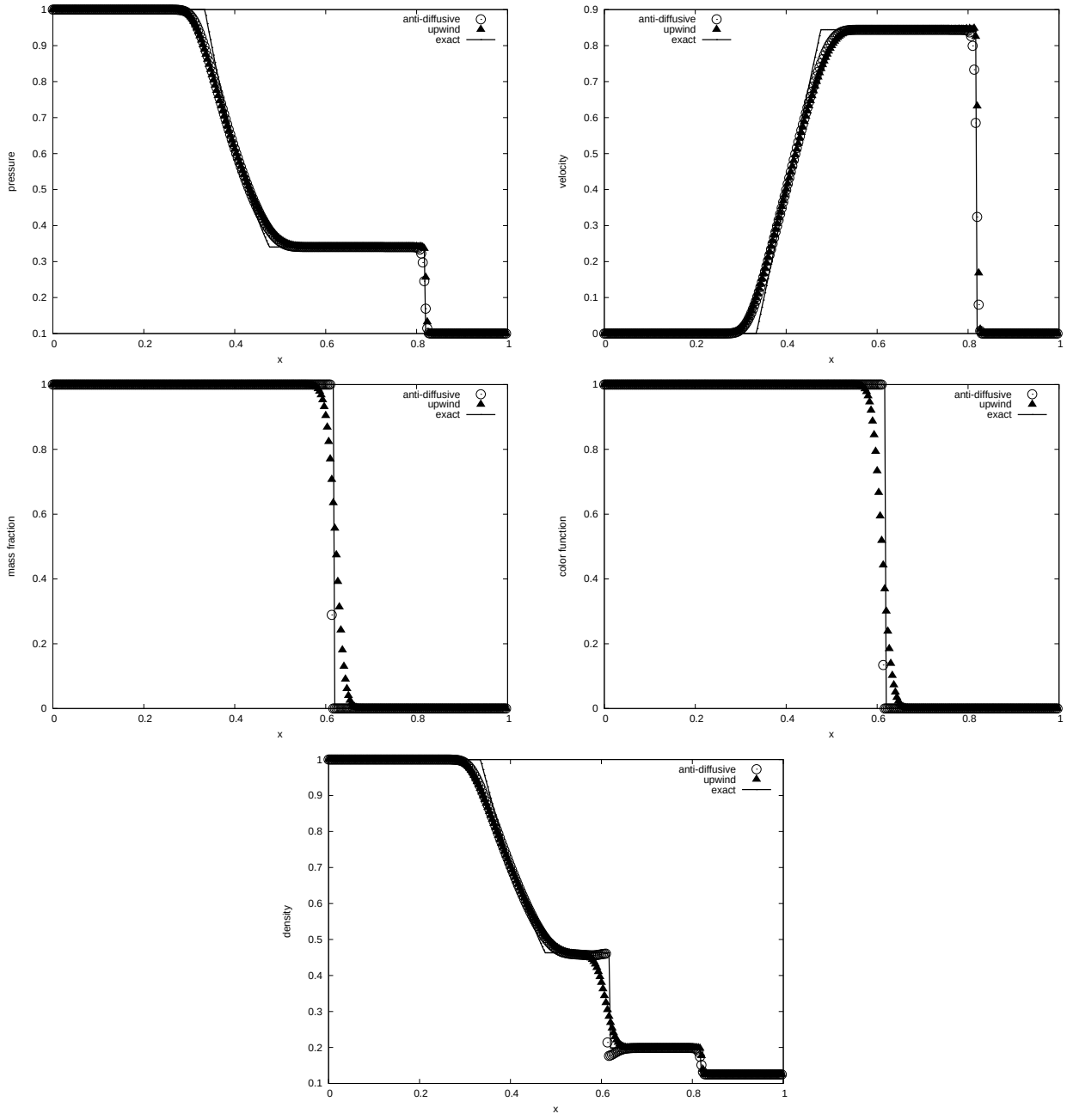

Figure 7: Profiles of the density, the pressure, the velocity, the mass fraction and the color function for the shock tube test obtained with the upwind scheme. the anti-diffusive scheme and the exact solution, at instant $t = 0.14\,\mathrm{s}$, with a 300 cells mesh.

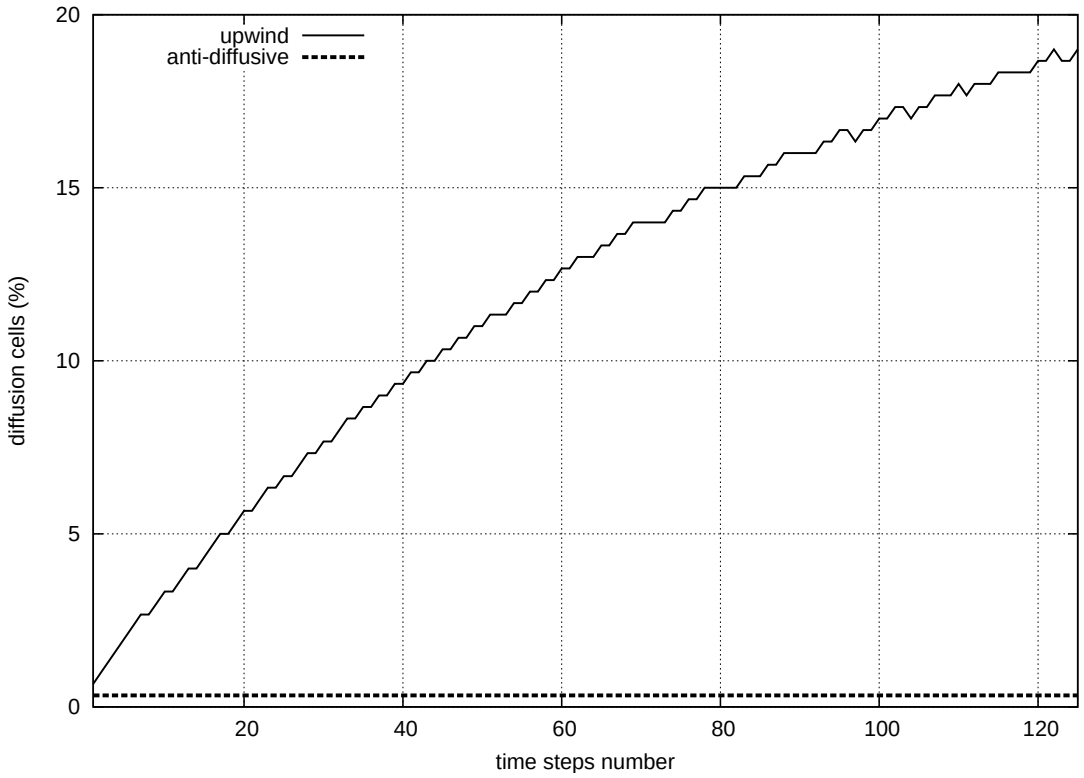

Figure 8: Shock Tube Test. Percent of cells in the domain where the color function z is numerically diffused versus the number of time steps for both upwind and anti-diffusive scheme.

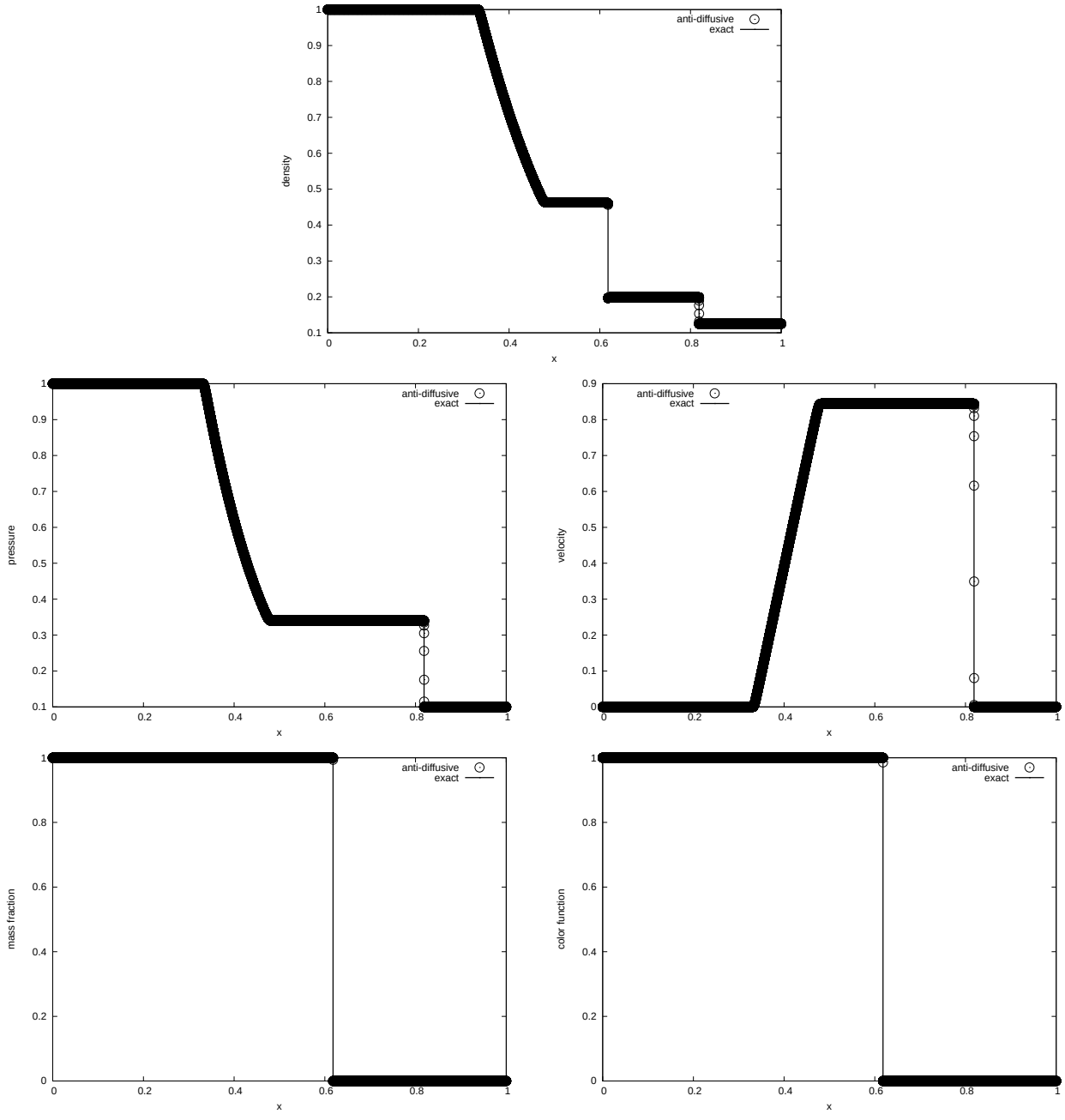

Figure 9: Profiles of the density, the pressure, the velocity, the mass fraction and the color function for the shock tube test obtained with the anti-diffusive scheme and the exact solution, at instant $t = 0.14\,\mathrm{s}$, with a 50 000 cells mesh.

5.3. Convergence Test

The shock tube test of section 5.2 is now used to investigate the convergence rate of the anti-diffusive scheme. As this test involves a weak solution of the system, we cannot expect a real evalution of a convergence order in the classical sense of Finite Differences. Nevertheless, we can evaluate a convergence rate of the scheme by estimating numerically the relative error of the computed solution in $L^1(0,1)$ norm for different space steps. Let q be a computed variable, we note q^{exact} the exact solution and $q_{\Delta x}$ the approximated solution computed on a Δx space step mesh. The $L^1(0,1)$ relative error $E_{\Delta x}[q]$ for the variable q and the space step Δx is defined by

$$t \mapsto E_{\Delta x}[q](t) = \frac{\|q^{\text{exact}}(\cdot,t) - q_{\Delta x}(\cdot,t)\|_{L^1(0,1)}}{\|q^{\text{exact}}(\cdot,t)\|_{L^1(0,1)}}.$$

Figure 10 displays the relative error in log scale for the variables ρ, u, P, y and z at instant $t = 0.14\,\text{s}$ within the range of space steps $\Delta x \in \{300, 500, 1000, 5000, 8500, 10000, 15000, 20000, 30000, 50000\}$. We computed the value of the convergence rates by performing a simple linear regression on the function $\ln(\Delta x) \mapsto \ln(E_{\Delta x}[q](t = 0.14))$, for $q \in \{\rho, P, u, z, y\}$ using PYTHON and the `polyfit` function of the `numpy` package. Results are gathered in table 1. Both table 1 and figure 10 provide interesting informations

Variable	Convergence rate for the upwind scheme	Convergence rate for the anti-diffusive scheme
Pressure	0.819	0.830
Velocity	0.824	0.835
Density	0.819	0.656
Mass Fraction y	0.478	1.042
Color Function z	0.525	1.038

Table 1: Convergence rate estimates obtained with both upwind and anti-diffusive schemes, for the shock tube test of section 5.2 at instant $t = 0.14\,\text{s}$. The rates are computed thanks to a linear regression performed on the function $\ln(\Delta x) \mapsto \ln(E_{\Delta x}[q](t = 0.14))$, $q \in \{\rho, P, u, z, y\}$.

regarding the anti-diffusive scheme compared to the classical upwind scheme. Indeed, for the variables that are "blind" to the contact discontinuity wave strength — namely the pressure and the velocity — there is very little difference between both schemes: the convergence error is just slightly lower, but the convergence rates are quite similar. However, the error for the variables y and z which purely transport the material interface is reduced by more than one decade for small values of Δx. Moreover, while the convergence for the mass fraction and the color function seem to reach a rate close to 0.5 for the upwind scheme, the anti-diffusive scheme converges with rates apparently closer to 1 for these variables. This convergence improvement also impacts the density variable that is sensitive to every wave of the system. The convergence of ρ is clearly improved for small values of Δx and the gain is also clear for the convergence rate as seen in table 1.

5.4. 2D Advection Test

The present simuation aims at testing the ability of the anti-diffusive scheme to deal with pure interface advection test in a 2D case. We consider a $1\,\text{m} \times 1\,\text{m}$ square domain that contains two perfect gases whose

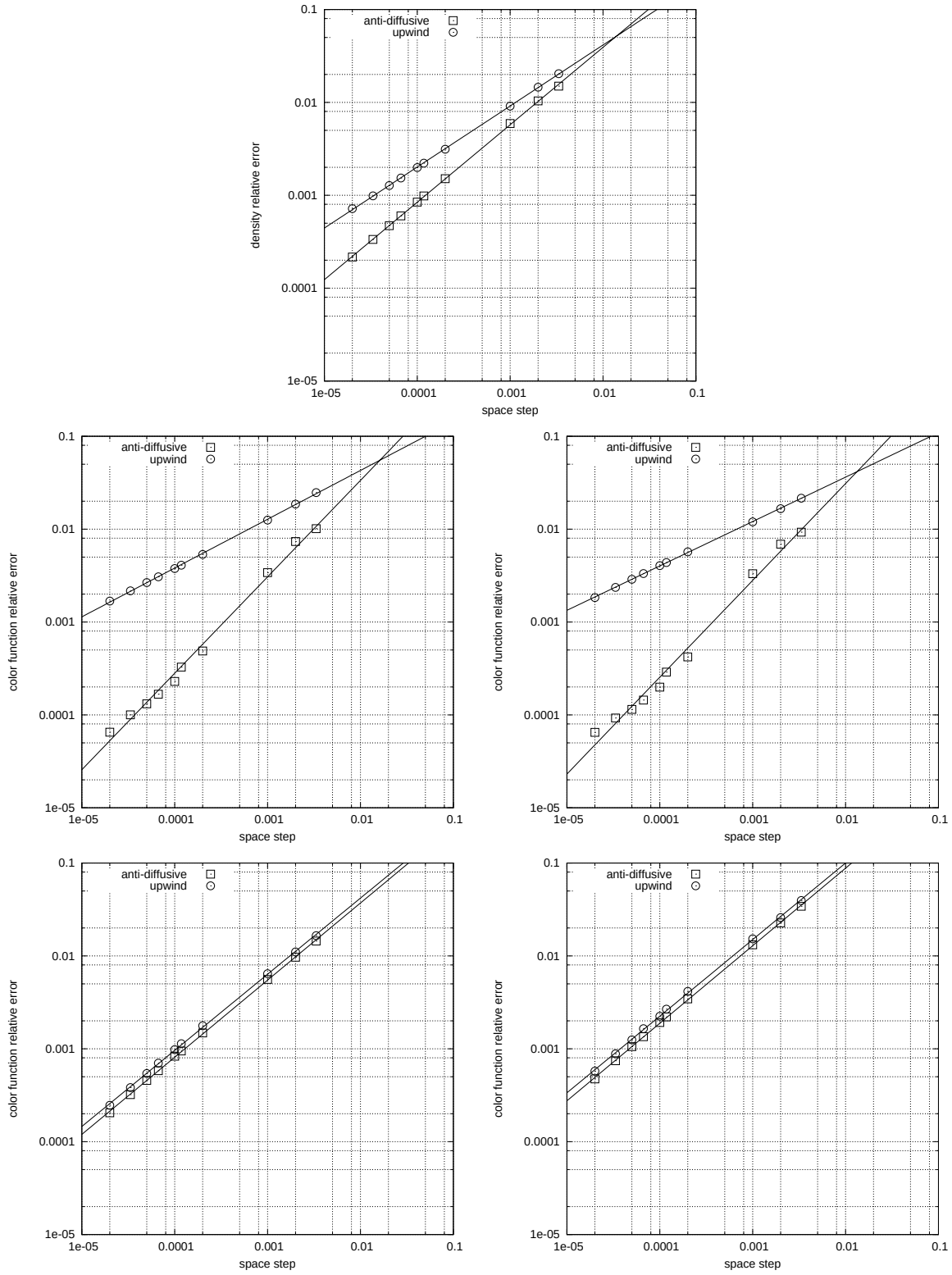

Figure 10: Relative error with respect to the time step obtained with the anti-diffusive and the upwind scheme for the shock tube test of section 5.2 at instant $t = 0.14\,\mathrm{s}$. All graphs are plotted using a log scale.

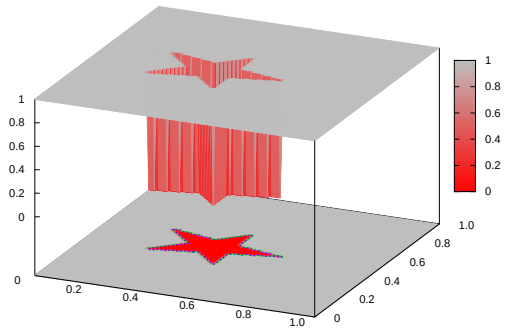

Figure 11: 2D Advection Test. Profile of the color function at $t = 0\,\mathrm{s}$

EOS verify relation (41). Initially both gases are separated by a star shaped interface as follows: let us define

$$\mathscr{A}_1 = \left\{(x_1, x_2) \in [0,1]^2 \text{ such that } \frac{1}{3} - \left|x_1 - \frac{1}{2}\right| < x_2 < \frac{2}{3} - 4\left|x_1 - \frac{1}{2}\right|\right\},$$
$$\mathscr{A}_2 = \left\{(x_1, x_2) \in [0,1]^2 \text{ such that } \frac{1}{3} - \left|x_1 - \frac{1}{2}\right| < x_2 < \frac{1}{2}\right\},$$
$$\mathscr{A} = \mathscr{A}_1 \cup \mathscr{A}_2.$$

At $t = 0$ we set

$$(\gamma, \rho) = (4.4, 10.0), \qquad \text{for } x \in \mathscr{A},$$
$$(\gamma, \rho) = (1.4, 0.01), \qquad \text{for } x \notin \mathscr{A}.$$

The pressure P and the velocity field $\mathbf{u} = (u_1, u_2)$ are initially uniform and set as follows

$$P(t = 0) = 1, \quad (u_1, u_2)(t = 0) = (\sqrt{2}/2, \sqrt{3}/2).$$

The computations are performed on a 100×100 mesh with periodic boundary conditions. The chosen mesh is rather coarse in order to see more clearly and rapidly the numerical diffusion effects on the interface. The initial discretized star shaped that gives the initial profile of the color function is depicted in figure 11. The uniform pressure and velocity fields set the star shaped interface in an uniform translation motion across the domain.

The simulation was performed with both classical upwind Lagrange-Remap scheme, and the anti-diffusive scheme. Figure 12 shows a comparison of the color function profile obtained with each of these schemes. At $t = 1.0\,\mathrm{s}$, while the interface shape computed by the anti-diffusive scheme clearly keeps its initial star shape, the upwind scheme already severely alters and diffuses the interface. At instant $t = 7.0\,\mathrm{s}$, the shape of the interface has totally disappeared with the upwind scheme but the anti-diffusive scheme succeeds quite well in preserving the initial shape of the interface.

The evolution of the number of diffusion cells for the color function has been measured for this test along the same lines as in for the test of section 5.1. The results are displayed in figure 13. As expected, the

number of numerical diffusion cells for the interface quickly reaches 100 % with the upwind scheme after less than 2 000 time steps. After 10 000 time steps, the percentage of diffused cells is only 3.75% for the anti-diffusive scheme.

We can also verify the good behaviour of the anti-diffusive scheme regarding the preservation of uniform pressure and velocity profiles. Indeed, we can see in figure 14 that the pressure and the velocity calculated by the anti-diffusive scheme remain uniform and constant throughout the motion. Moreover, the anti-diffusive feature is also effective for both density ρ and mass fraction variables y as shown in figure 15.

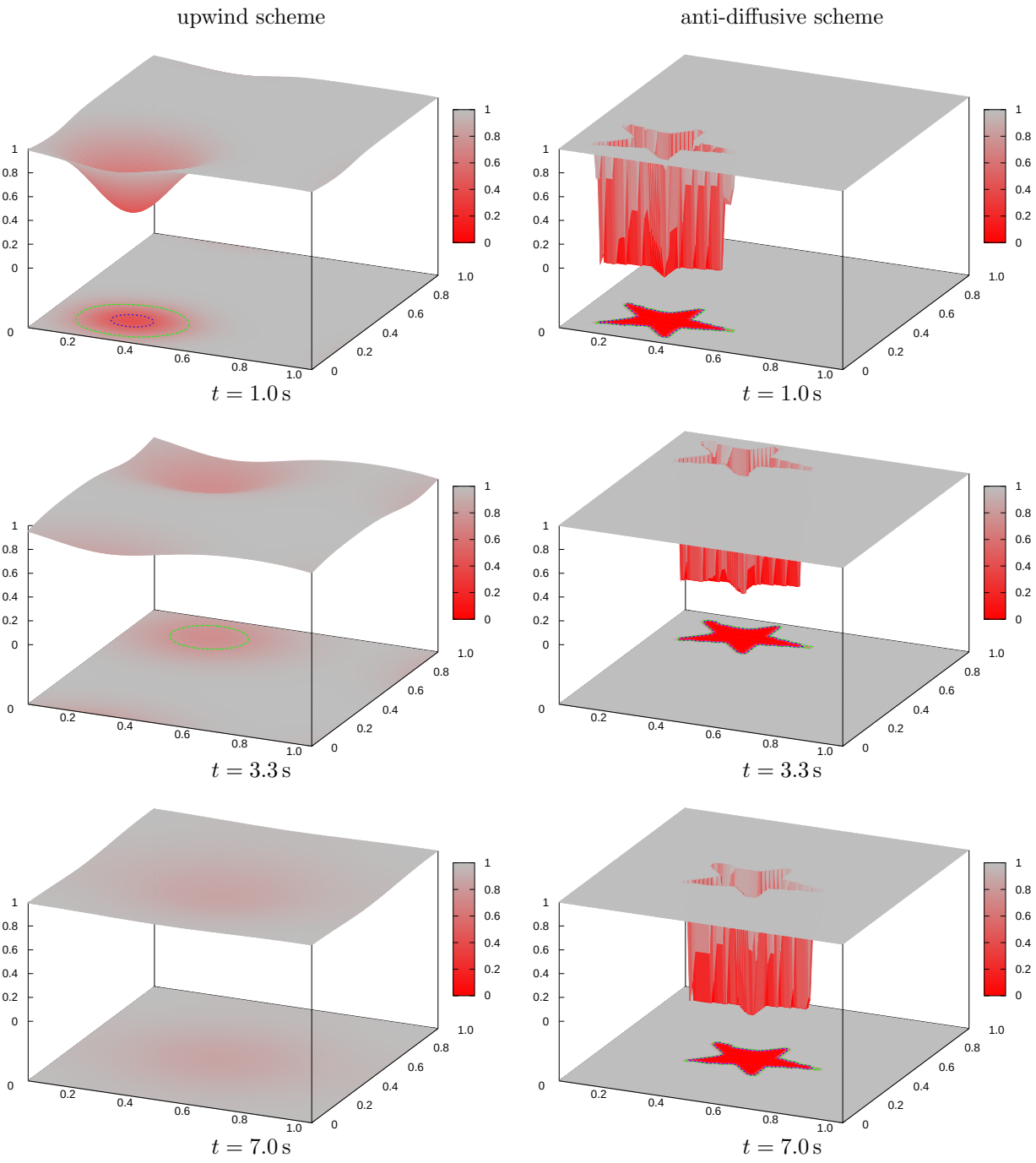

Figure 12: 2D Advection Test. Profiles of the color function obtained with the upwind scheme and the anti-diffusive scheme at instant $t \in \{1.0, 3.3, 7.0\}\,\mathrm{s}$

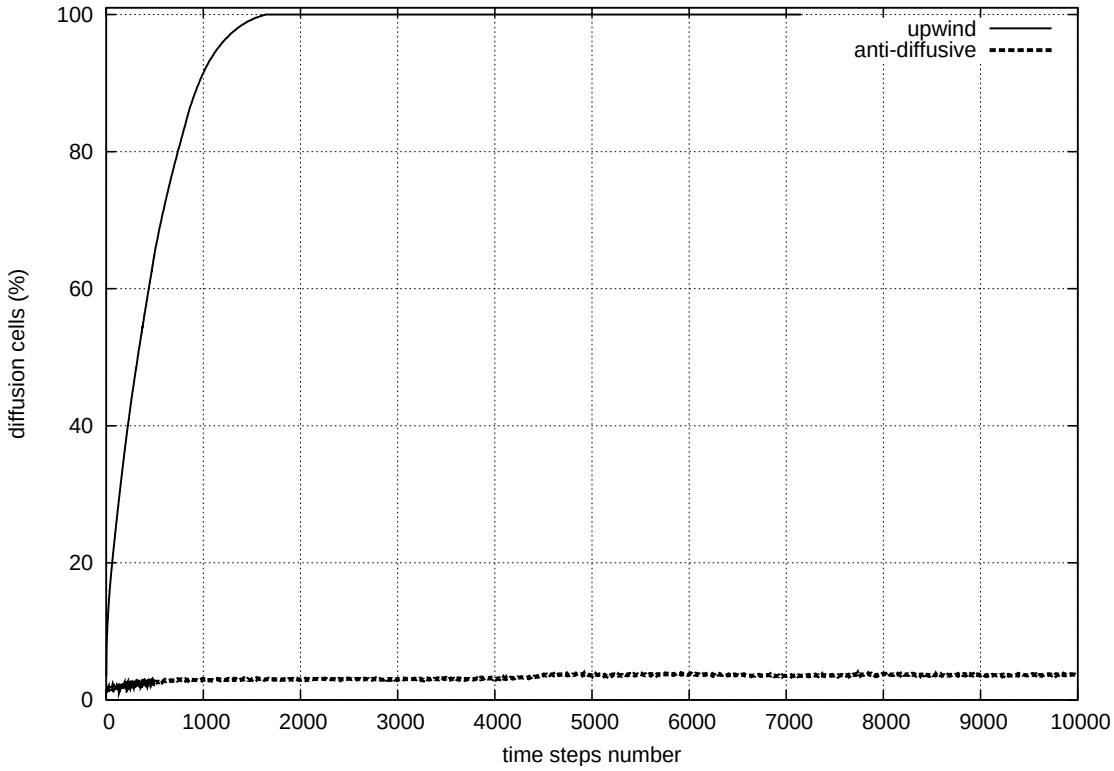

Figure 13: 2D Advection Test. Percent of cells in the domain where the color function z is numerically diffused versus the number of time steps, for the upwind the and the anti-diffusive scheme.

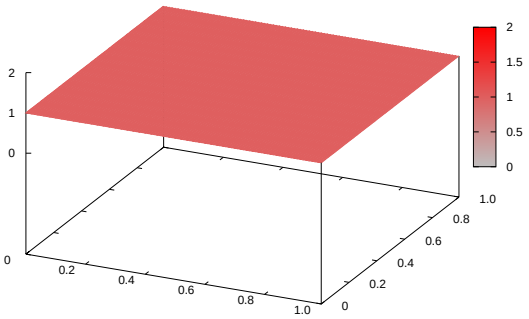

Pressure

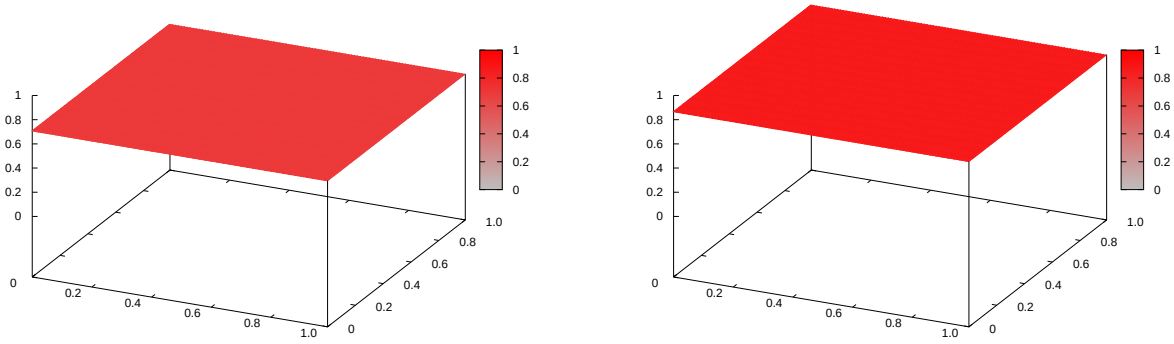

Velocity component u_1 Velocity component u_2

Figure 14: 2D Advection Test. Profiles of the pressure and the velocity components u_1, u_2 obtained with the anti-diffusive scheme at instant $t = 7.0\,\mathrm{s}$

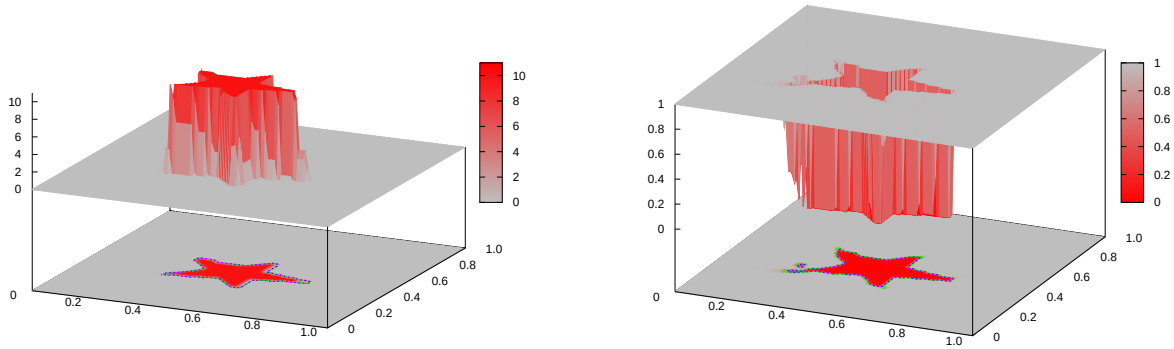

Density Mass Fraction

Figure 15: 2D Advection Test. Profiles of the density ρ and mass fraction y obtained with the anti-diffusive scheme at instant $t = 7.0\,\mathrm{s}$

5.5. Shock/Bubble Interaction Test

We now present a 2D test that consists in simulating the impact of a shock travelling through air onto a helium bubble. This test is an adaptation of the experiment achieved in [10] and similar simulations are available in [1, 19, 22, 8, 26, 3, 29]. The initial conditions are depicted in figure 16: a bubble of helium is surrounded by air within a $L_1 \times L_2$ rectangular domain. At $t = 0$, the bubble is at rest and has a circular shape whose center is located at (X_1, X_2). We denote by r the initial radius of the bubble. The planar shock is initially located at $x_1 = L_s$ and moves from left to right towards the bubble. The parameters chosen for this test are

$$L_1 = 267 \times 10^{-3}\,\mathrm{m}, \qquad L_2 = 89 \times 10^{-3}\,\mathrm{m}, \qquad L_s = 15 \times 10^{-3}\,\mathrm{m},$$
$$X_1 = 84.33 \times 10^{-3}\,\mathrm{m}, \qquad X_2 = 44.5 \times 10^{-3}\,\mathrm{m}, \qquad r = 25 \times 10^{-3}\,\mathrm{m}.$$

Both air and helium are modelled by two perfect gases whose coefficients γ and initial states are given in table 2. The domain is discretized with a 900×300 regular mesh. Top and bottom boundary conditions are set to solid walls while we use transparent boundary conditions for the left and right boundaries.

location	density (kg.m^{-3})	pressure (Pa)	u_1 (m.s^{-1})	u_2 (m.s^{-1})	γ
air (post-shock)	1.376363	1.56980×10^5	394.728	0	1.4
air (pre-shock)	1.0	10^5	0	0	1.4
helium	0.181875	10^5	0	0	1.648

Table 2: Shock/Bubble Interaction Test. EOS coefficients and initial data.

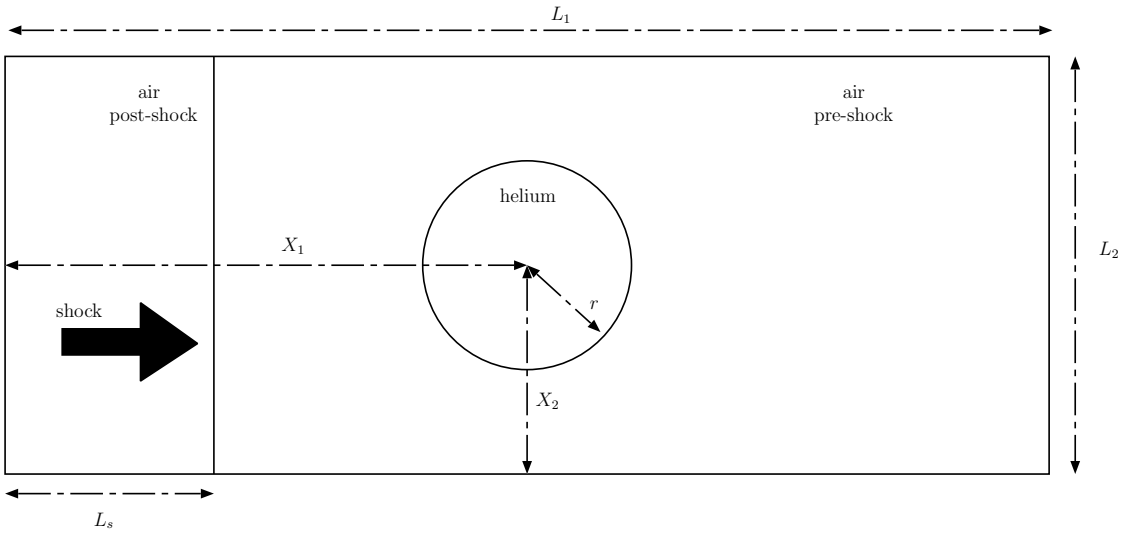

Figure 16: Shock/Bubble Interaction Test. Description of the initial conditions.

The shock reaches the bubble which gains speed and looses its circular shape. Figure 17 displays the evolution of the shape of the bubble obtained with both the anti-diffusive and the upwind solver. Let us

underline that these profiles are obtained thanks to a mapping of the values of the color function z and do not involve any interface reconstrution post-treatment or iso-contours computation. One can see that there is a very good agreement between both schemes regarding the overall shape and location of the bubble throughout the simulation. The numerical diffusion seems totally confined in a very thin layer of cells for the anti-diffusive scheme. This allows to capture fine interface details such as the long filament that appears on the right side of the bubble after it gets compressed by the shock wave. The percent of cells containing a numerically diffused value of z is displayed in figure 19. Compared to the upwind scheme, the growth rate of the diffused cells percentage is lowered by at least a decade for the anti-diffusive scheme. After 2600 time steps, the diffusion percent is 26.2 % with the upwind scheme, while it is only 0.81 % with the anti-diffusive solver. Although this percentage remains very low for the anti-diffusive solver, it keeps growing as the number of time steps increases. In our opinion this can be partly explained by the fact that the interface of the bubble gets stretched by the motion. Thus the perimeter of the interface increases which implies that the number of diffusion cells surrounding the interface increases as well. As shown in figure 18, the anti-diffusive property of the solver also acts on the mass fraction y. For this variable the anti-diffusive and the upwind schemes show a good agrement with each other regarding the shape and the location of the interface.

Although we are dealing with richer wave patterns and interactions, the behaviour of the anti-diffusive scheme is quite coherent with what we observed for the shock tube test in section 5.2. Figure 20 presents the pressure profiles at $t = 2.85 \times 10^{-4}\,\mathrm{s}$. We also plotted several iso-contours for the sake of comparison between both schemes. The schemes show very little difference in computing the pressure variable. Figure 21 shows the profiles of the pressure along the axis $x_2 = 44.5 \times 10^{-3}\,\mathrm{m}$, and we can observe a strong agreement between the solutions provided by both schemes.

Let us now turn to the density variable. We present in figure 22 a mapping of the density variable along with several density iso-contours. Once again the results concur with those of section 5.2: the approximated density computed with the anti-diffusive scheme is very sharp across the interface, while the upwind scheme shows a diffused profile. The profile of the shock for the density variable seems equivalent for both schemes. Moreover, apart from regions close to the interface, the density iso-contours appear to be similar. Figure 23 displays a cut of the density variable across the axis $x_2 = 44.5 \times 10^{-3}\,\mathrm{m}$. The results once again agree with the shock tube test of section 5.2. The interface is printed onto the density variable using only two or three diffusion cells with the anti-diffusive solver, while it is diffused across several cells for the upwind scheme. At instant $t = 0.57 \times 10^{-3}\,\mathrm{s}$, we can see that the anti-diffusive scheme succeeds in capturing the interface within a very thin zone when the interface is totally diffused by the upwind scheme. Finally we present in figure 24 the Schlieren diagrams obtained with both simulations, namely the mapping of $|\mathrm{grad}\rho|$ in the computational domain at $t = 2.85 \times 10^{-4}\,\mathrm{s}$. The wave propagation phenomena also appear very similar in these diagrams. Let us emphasize that these pictures do not display any iso-contours: the very sharp

contour that reveals the location of the interface with the anti-diffusive results has been obtained by the sole computation of $|\text{grad}\rho|$ values.

5.6. Kelvin-Helmoltz Test

We finally test the anti-diffusive scheme with the simulation of a Kelvin-Helmoltz instability. We consider a $1\,\text{m} \times 1\,\text{m}$ square domain containing two perfect gases separated by an interface Γ. We define Γ as perturbation of the line $x_2 = 1/2$ within the zone $x_1 \in [\alpha, \beta]$, where $0 < \alpha < \beta < 1$. The perturbation is defined by the iso-contour $f(x_1, x_2) = 0$, where the function f reads

$$f(x_1, x_2) = \begin{cases} x_2 + K \sin\left[\pi\left(\frac{x_1-\alpha}{\beta-\alpha}\right)\right], & \text{if } x_1 \in [\alpha, \beta] \\ 1/2, & \text{if } x_1 \notin [\alpha, \beta] \end{cases}.$$

For our test, we chose the parameters

$$\alpha = 0.65, \qquad \beta = 0.85, \qquad K = 0.03.$$

At $t = 0$, the flow configuration is given by

$$(\gamma, \rho, P, u_1, u_2) = (1.4, 1.0, 0.71, +0.25, 0.0), \quad \text{if } f(x_1, x_2) > 0,$$
$$(\gamma, \rho, P, u_1, u_2) = (1.67, 1.0, 0.71, -0.25, 0.0), \quad \text{if } f(x_1, x_2) \leq 0.$$

The computational domain is discretized over a 1000×1000 cells mesh and we set periodic boundary conditions for the left and right boundaries. Both top and bottom boundaries are solid walls. This test is meant to challenge the ability of the anti-diffusive scheme to deal with very complex variations of the interface geometry while keeping control of the numerical diffusion for the variable z.

Figures 5.6, 5.6,5.6, 5.6 provide a mapping of the color function values for both anti-diffusive and upwind schemes at several instants. The velocity differential creates a shearing effect that first streches the perturbation of the interface. This triggers the instability and the interface starts winding around itself. One can see that the overall aspect of the instability is similar with both schemes. However, in regions where the upwind scheme generates numerical values for z such that $0 < z < 1$, one can see that that anti-diffusive scheme creates very fine interface structures that are not destroyed by the numerical diffusion. Moreover, when numerical diffusion seems to extend within the central vortex for the anti-diffusive scheme, it seems to decrease again after few time steps. Let us emphasize that we do not claim that the filaments appearing in the anti-diffusive results are more physical than the shapes obtained with the updwind scheme. Neither do we suggest that the solution has a better resolution — in the sense of a more converged solution — with the anti-diffusive scheme. Indeed, there is no reason to suppose that the velocity field computed by the anti-diffusive scheme is better a resolved velocity field and describes finer vortices than the velocity field computed with the upwind scheme.

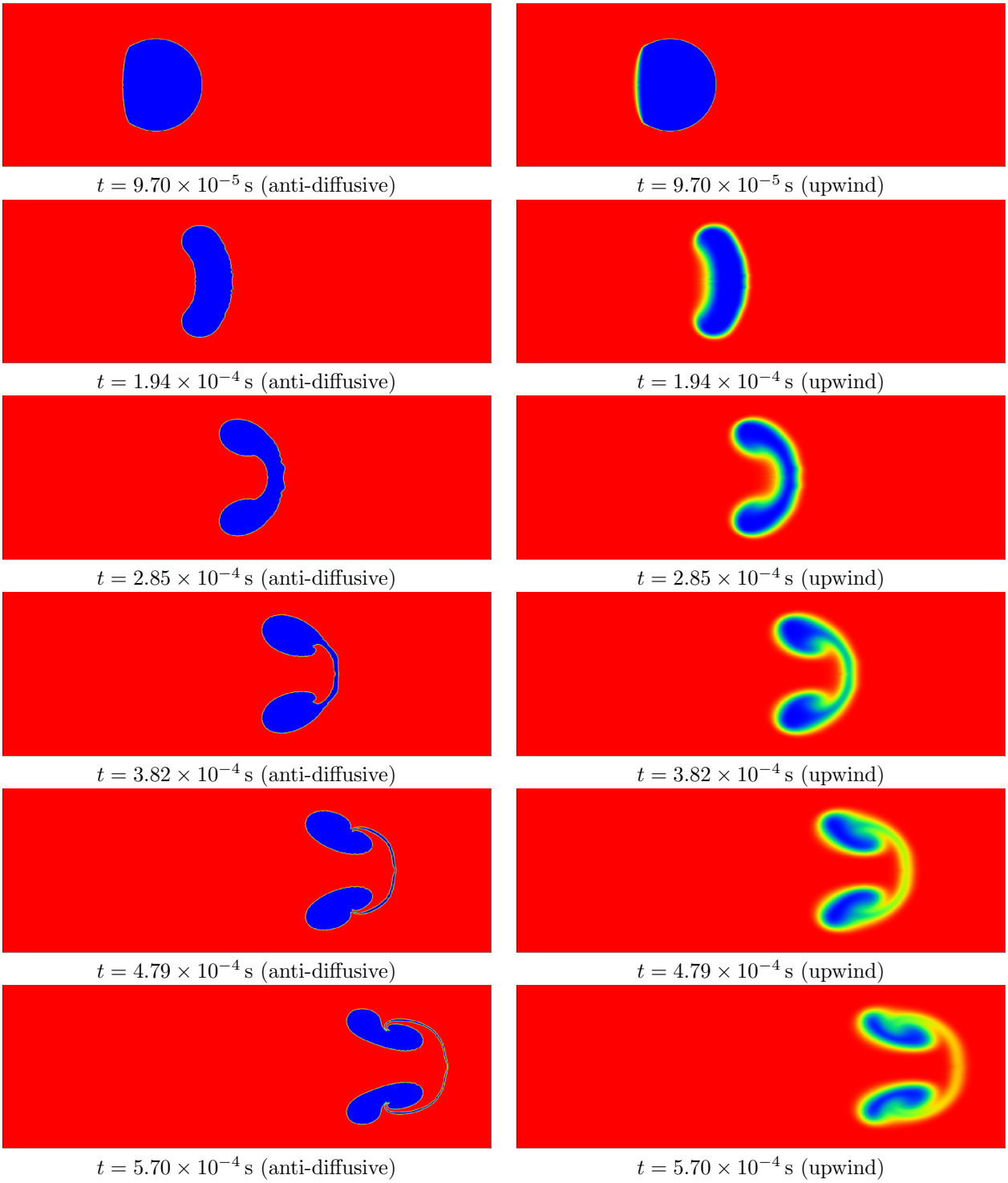

Figure 17: Shock/Bubble Interaction Test. Mapping of the color function z for both upwind and anti-diffusive solvers.

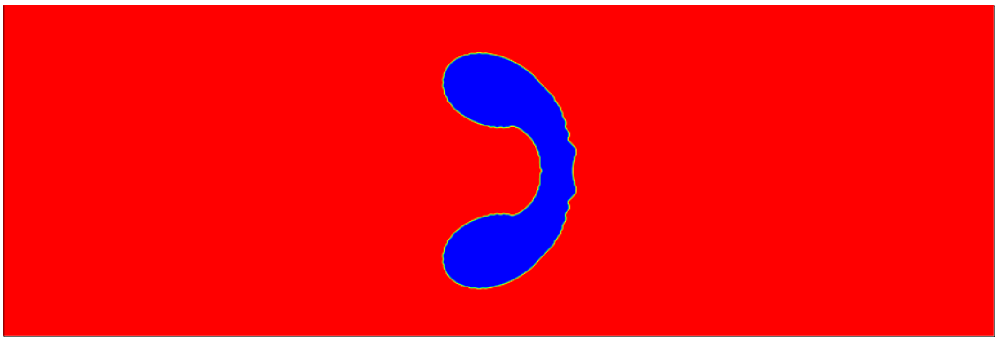

anti-diffusive

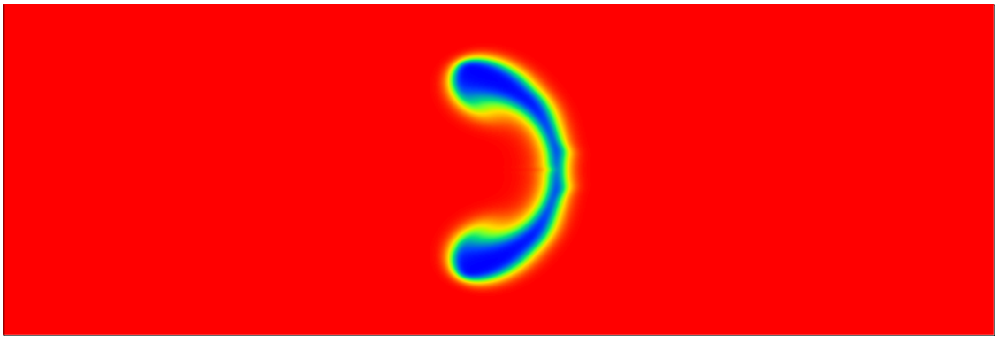

upwind

Figure 18: Shock/Bubble Interaction Test. Mapping of the mass fraction y for both upwind and anti-diffusive solver at instant $t = 2.85 \times 10^{-4}$s.

We present the percent of numerically diffused cells in figure 5.6. As in the previous tests, we see that the anti-diffusive solver succeeds in controling the diffusion of the color function z. After 11 000 time steps the percent of cells with numerically diffused value of z in the domain is 7.54 % for the anti-diffusive scheme and 59.71 % for the upwind scheme. As in section 5.5, we explain the growing trends of this percent by the fact that the perimeter of the interface keeps increasing as the instability grows, generating thus more diffusion cells. For sake of comparison, we also plotted the evolution of the kinetic energy in the direction x_2 perpendicular to the shear: figure 5.6 displays the graph of the function $t \mapsto \int_{[0,1]\times[0,1]} \frac{1}{2}\rho u_2^2(x_1, x_2, t)\mathrm{d}x_1\mathrm{d}x_2$. This function provides comparison elements concerning the growth rate of the instability computed by both schemes. Once again, one can see that there is a strong match between both approximated solutions, even for large value of t, far from the linear growth regime.

6. Conclusion

We presented a Lagrange-Remap solver for the five-equation model with isobaric closure examined in [2, 3]. This solver was designed following similar lines to [13, 6, 7]. This method allows to contain the numerical diffusion affecting the color function z that defines the location of the interface between both fluids. Our algorithm does not involve any interface reconstruction process and does not generate extra CPU costs

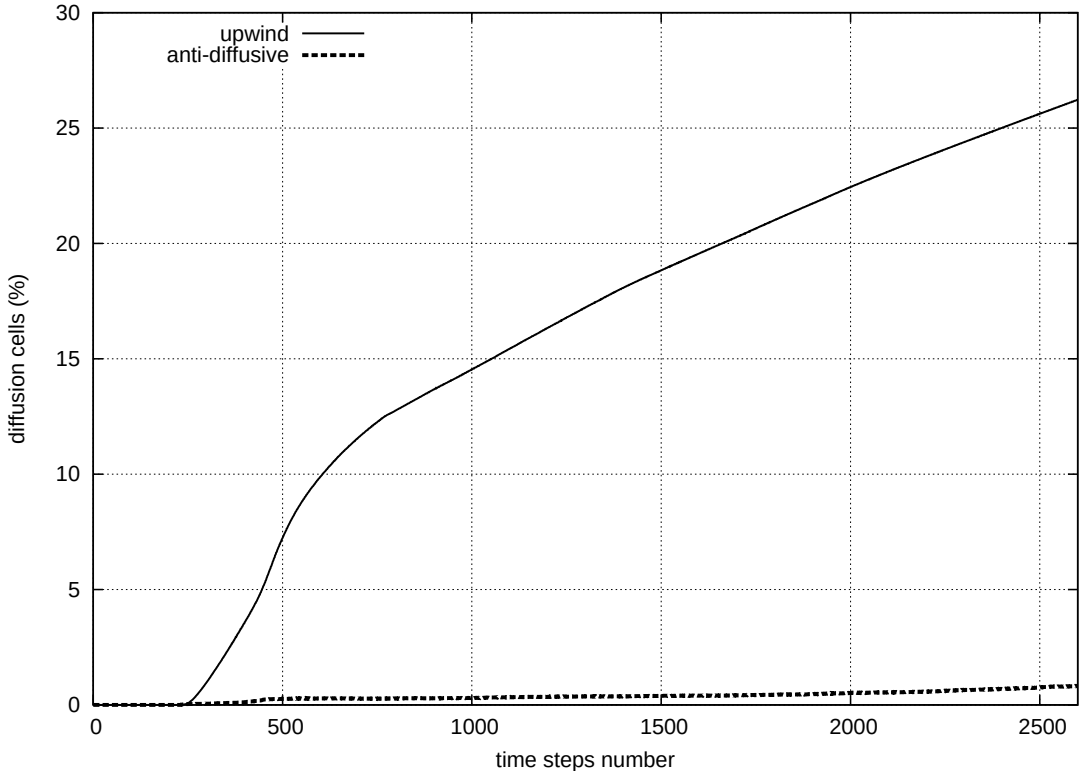

Figure 19: Shock/Bubble Interaction Test. Percent of cells in the domain where the color function z is numerically diffused versus the number of time steps for both upwind and anti-diffusive scheme.

compared to the classical Lagrange-Remap upwind solver. This numerical method does not rely on the analytical form of the EOSs and allows a straightforward use of complex EOSs. The numerical solver is conservative with respect to the mass, momentum, total energy, and partial masses. The numerical fluxes implemented within this scheme are consistent by construction. Under a classical CFL condition, the solver is endowed with stability properties for the color function z and the mass fraction y that are similar to the stability properties of the upwind scheme. In particular, we demonstrated positivity properties regarding both mass fraction and color function. We prooved that the numerical scheme preserves constant pressure and velocity profiles similar to those examined in [2, 3].

We performed 1D and 2D numerical tests that showed that the discretization of the interface is resolved within a very few transition cells. We verified throughout the tests that the anti-diffusive mechanism is also active for other variables experiencing a jump across the interface like the mass fraction and the density. Far from the interface, the anti-diffusive solver seems to degenerate to the classical Lagrange-Remap upwind. A convergence test was performed on a shock tube test that indicates that the convergence rate of the anti-diffusive solver is at most order 1. Numerical tests involving tabulated EOSs were also achieved. By means of a simple dimensional splitting, we performed two-dimensional tests that concur with the one-dimensional results. Indeed, we observed a good control of the numerical diffusion in the vicinity of the interface and a strong agreement with the upwind solver far from the interface.

The anti-diffusive solver has already been successfully implemented in a three-dimensional parallelized code that is in the process of validation. An extension of the numerical method involving higher order methods is in progress.

References

[1] R. Abgrall. How to prevent pressure oscillations in multicomponent flow calculations: a quasi-conservative approach. *J. Comp. Phys.*, 125:pp. 150–160, 1996.

[2] G. Allaire, S. Clerc, and S. Kokh. A five-equation model for the numerical simulation of interfaces in two-phase flows. *C. R. Acad. Sci. Paris, Série I*, t. 331:pp. 135–140, 2000.

[3] G. Allaire, S. Clerc, and S. Kokh. A five-equation model for the simulation of interfaces between compressible fluids. *J. Comput. Phys.*, 181(2):pp. 577–616, 2002.

[4] B. Després. Inégalité entropique pour un solveur conservatif du système de la dynamique des gaz en coordonnées de lagrange. *C. R. Acad. Sci. Paris, Série I*, 324:1301–1306, 1997.

[5] B. Després and F. Lagoutière. Un schéma non-linéaire anti-dissipatif pour l'équation d'advection linéaire. *C. R. Acad. Sci. Paris, Série I*, t. 328:pp. 939–944, 1999.

[6] B. Després and F. Lagoutière. Contact discontinuity capturing schemes for linear advection and compressible gas dynamics. *J. Sci. Comp.*, 16(4):479–524, 2001.

[7] B. Després and F. Lagoutière. Numerical resolution of a two-component compressible fluid model with interfaces. *Progress in Comp. Fluid Dynamics*, 7(6):295–310, 2007.

[8] R. Fedkiw, T. Aslam, B. Merriman, and S. Osher. A non-oscillatory Eulerian approach to interfaces in multimaterial flows (the ghost fluid method). *J. Comp. Phys.*, 152:p. 457, 1999.

[9] E. Godlewski and P.-A. Raviart. *Numerical approximation of hyperbolic systems of conservation laws*, volume 118 of *Applied Mathematical Sciences*. 1996.

[10] J.F. Haas and B. Sturtevant. Interaction of a weak shock wave with cylindrical and spherical gas inhomogeneities. *J. Fluid Mech.*, 181:pp. 41–76, 1987.

[11] S. Karni. Multicomponent flow calculations by a consistent primitive algorithm. *J. Comp. Phys.*, 112:pp. 31–43, 1994.

[12] S. Karni. Hybrid multifluid algorithms. *SIAM J. Sci. Comput.*, 17(5):pp. 1019–1039, 1996.

[13] F. Lagoutière. *Modélisation mathématique et résolution numérique de problèmes de fluides compressibles à plusieurs constituants*. PhD thesis, Université Paris VI, 2000.

[14] J. Massoni, R. Saurel, B. Nkonga, , and R. Abgrall. Proposition de méthodes et modèles eulériens pour les problèmes à interfaces entre fluides compressibles en présence de transfert de chaleur. *International Journal of Heat and Mass Transfer*, 45(6):pp. 1287–1307, 2001.
[15] A. Murrone and H. Guillard. A five equation reduced model for compressible two phase flow problems. *J. Comput. Phys.*, 202(2):pp. 664–698, 2005.
[16] S. Osher and P. Smereka. A level set approach for computing solutions to incompressible two-phase flow. *J. Comp. Phys.*, 114:pp. 146–159, 1994.
[17] D. Peng, B. Merriman, S. Osher, H. Zhao, and M. Kang. A PDE Based Fast Local Level Set Method. *J. Comp. Phys.*, 155:pp. 410–438, 1999.
[18] G. Perigaud and R. Saurel. A compressible flow model with capillary effects. *J. Comput. Phys.*, 209(1):139–178, 2005.
[19] J.J. Quirk and S. Karni. On the dynamics of a shock-bubble interaction. *J. Fluid Mech.*, 318:pp. 129–163, 1996.
[20] P.L. Roe. Approximate riemann solvers, parameter vectors, and difference schemes. *J. Comp. Phys.*, 43:pp. 357–372, 1981.
[21] R. Saurel and R. Abgrall. A multiphase godunov method for compressible multifluid and multiphase flows. *J. Comp. Phys.*, 150:pp. 425–467, 1999.
[22] R. Saurel and R. Abgrall. A simple method for compressible multifluid flows. *SIAM J. Sci. Comput.*, 21(3):pp. 1115–1145, 1999.
[23] J.A. Sethian. *Level set methods: evolving interfaces in geometry, fluid mechanics, computer vision and materials sciences.* 1996.
[24] J.A. Sethian. *Level Set Methods and fast marching methods: evolving interfaces in computational geometry, fluid mechanics, computer vision and materials science.* Cambridge University Press, Cambridge, 1999.
[25] K.M. Shyue. An efficient shock-capturing algorithm for compressible multicomponent problems. *J. Comp. Phys.*, 142:pp. 208–242, 1998.
[26] K.M. Shyue. A fluid-mixture type algorithm for compressible multicomponent flow with van der Waals equation of state. *J. Comp. Phys.*, 156:pp. 43–88, 1999.
[27] K.M. Shyue. A fluid-mixture type algorithm for compressible multicomponent flow with mie-gruneisen equation of state. *J. Comp. Phys.*, 171:pp. 678–707, 2001.
[28] J. Strain. Fast tree-based redistancing for level set computations. *J. Comp. Phys.*, 152:pp. 664–686, 1999.
[29] G. Allaire and S. Kokh. Test-case N° 19: Shock-bubble interaction. *Multiphase Science and Technology*, 16:pp. 117–120, 2004.
[30] O. Desjardins, V. Moureau, and H. Pitsch. An accurate conservative level set/ghost fluid method for simulating turbulent atomization. *J. Comp. Phys.*, 227:pp. 8395–8416, 2008.
[31] D. Henright, R. Fedkiw, J. Ferziger, and I. Mitchell. A hybrid particle level set method for improved interface capturing. *J. Comp. Phys.*, 183:pp. 83–116, 2002.
[32] S. Kokh and F. Lagoutière. An anti-diffusive method for simulating compressible two-phase flows with interfaces. In R. Eymard and J.M. Hérard, editors, *Finite Volumes for Complex Applications V*, pages pp. 519–526, 2008.
[33] T.G. Liu and C. Khoo. The accuracy of the modified ghost fluid method for gasgas riemann problem. *Applied Numerical Mathematics*, 57:pp. 721–733, 2007.
[34] T.G. Liu, C. Khoo, and K.S. Yeob. Ghost fluid method for strong shock impacting on material interface. *JCP*, 190:pp. 651–681, 2003.
[35] W. Mulder, S.Osher, and J.A. Sethian. Computing interface motion in compressible gas dynamics. *J. Comput. Phys.*, 100(2):pp. 209–228, 1992.
[36] D. Nguyen, F. Gibou, and R. Fedkiw. A fully conservative ghost fluid method & stiff detonation waves. In *12th Int. Detonation Symposium, San Diego, CA*, 2002.
[37] E. Olsson and G. Kreiss. A conservative level set method for two phase flow. *J. Comp. Phys.*, 210:pp. 225–246, 2005.
[38] E. Olsson, G. Kreiss, and S. Zahedi. A conservative level set method for two phase flow ii. *J. Comp. Phys.*, 225:pp. 785–807, 2007.
[39] G. Russo and P. Smereka. A remark on computing distance functions. *J. Comp. Phys.*, 163, 2000.
[40] G.A. Sod. A survey of several finite difference methods for systems of nonlinear hyperbolic conservation laws. *J. Comp. Phys.*, pages pp. 1–31, 1978.
[41] M. Sussman and E. Fatemi. An efficient, interface-preserving level set redistancing algorithm and its application to interfacial incompressible fluid flow. *SIAM J. Sci. Comput.*, 20:pp. 1165–1191, 1999.
[42] E.H. van Brummelen and B. Koren. A pressure-invariant conservative godunov-type method for barotropic two-fluid flows. *J. Comp. Phys.*, 185:pp. 289–308, 2003.

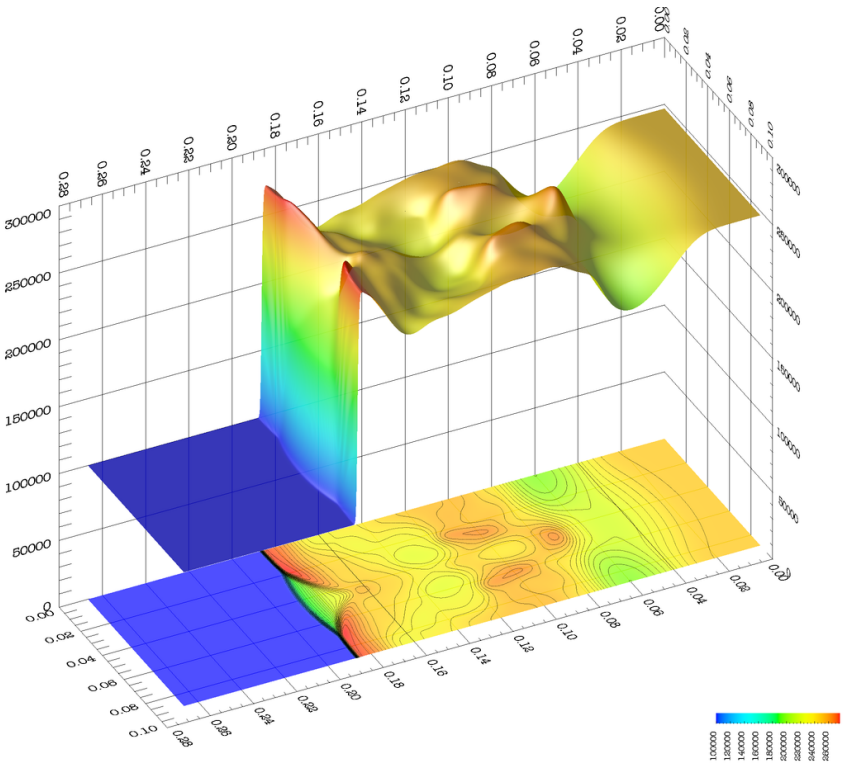

anti-diffusive solver

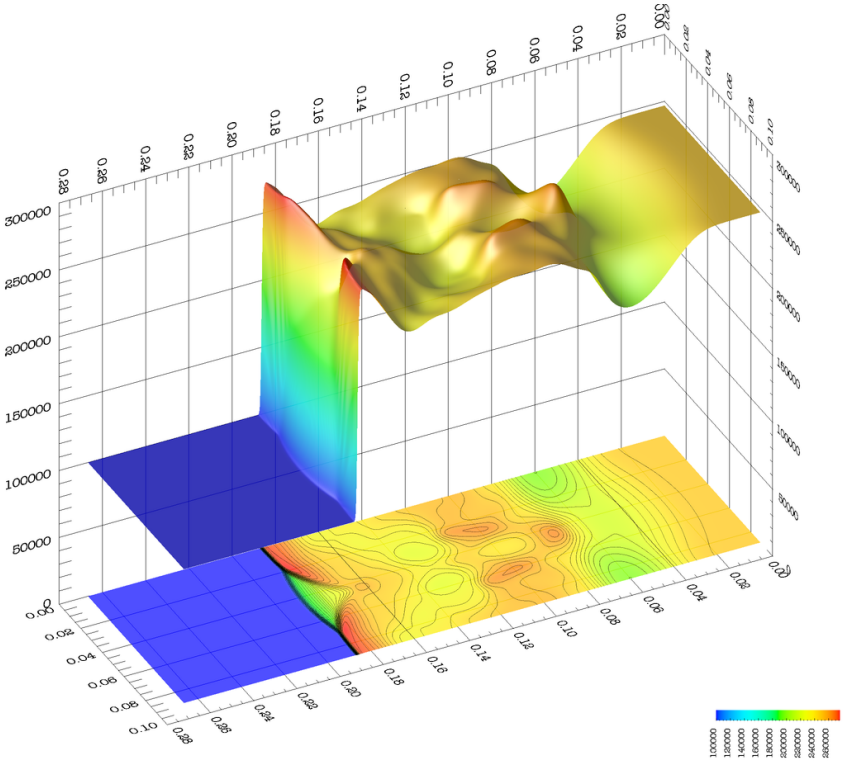

upwind solver

Figure 20: Shock/Bubble Interaction Test. Pressure profile for both upwind and anti-diffusive solver at instant $t = 2.85 \times 10^{-4}$s.

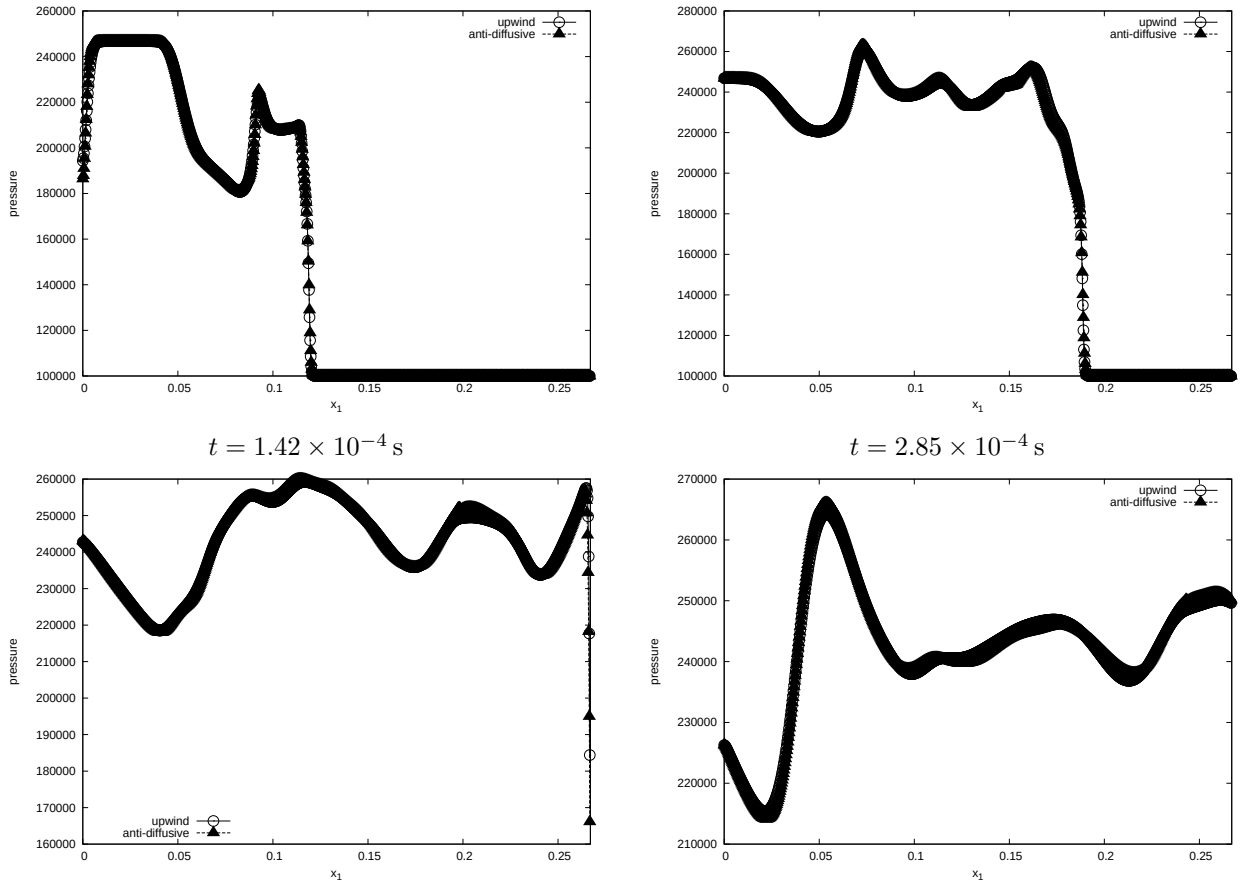

Figure 21: Shock/Bubble Interaction Test. Profile of the pressure along the axis $x_2 = 44.5 \times 10^{-3}\,\mathrm{m}$ with both upwind and anti-diffusive solvers.

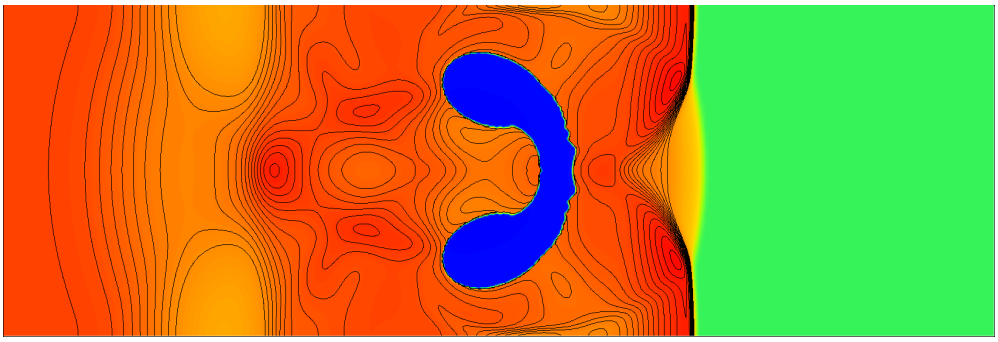

anti-diffusive

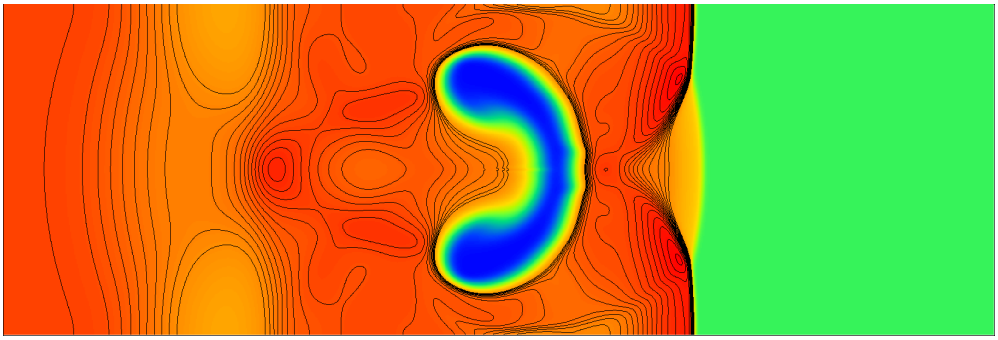

upwind

Figure 22: Shock/Bubble Interaction Test. Mapping of the density for both upwind and anti-diffusive solver at instant $t = 2.85 \times 10^{-4}$s.

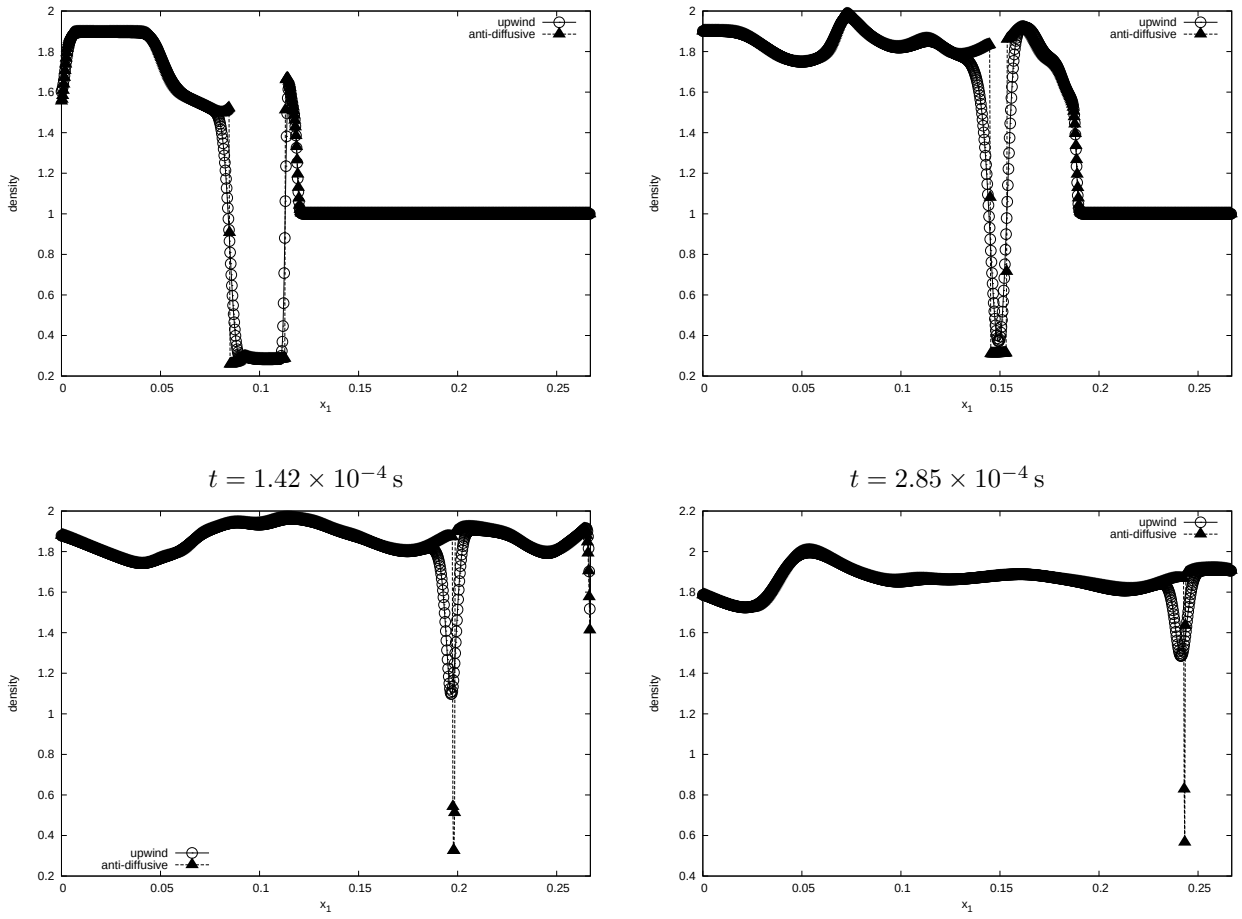

Figure 23: Shock/Bubble Interaction Test. Profile of the density along the axis $x_2 = 44.5 \times 10^{-3}\,\mathrm{m}$ with both upwind and anti-diffusive solvers.

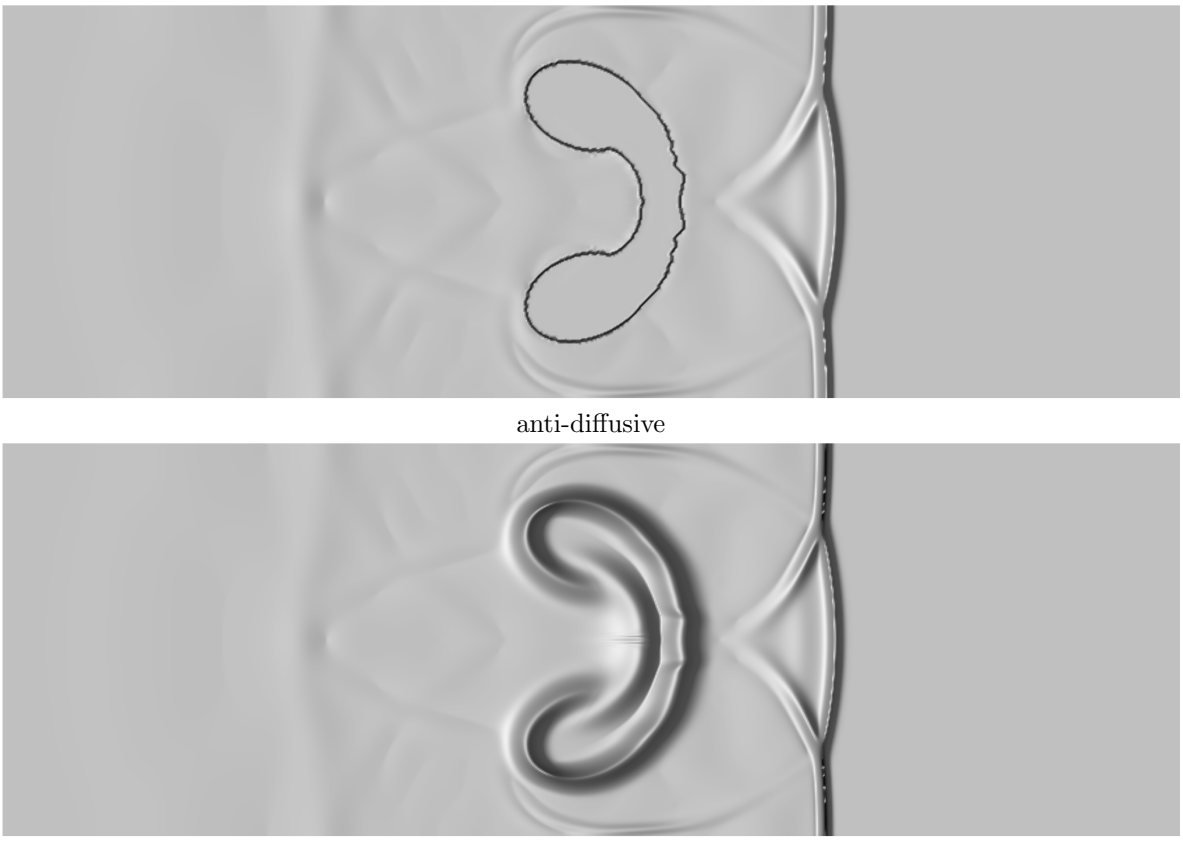

anti-diffusive

upwind

Figure 24: Shock/Bubble Interaction Test. Schlieren diagram for both upwind and anti-diffusive solver at instant $t = 2.85 \times 10^{-4}$s.

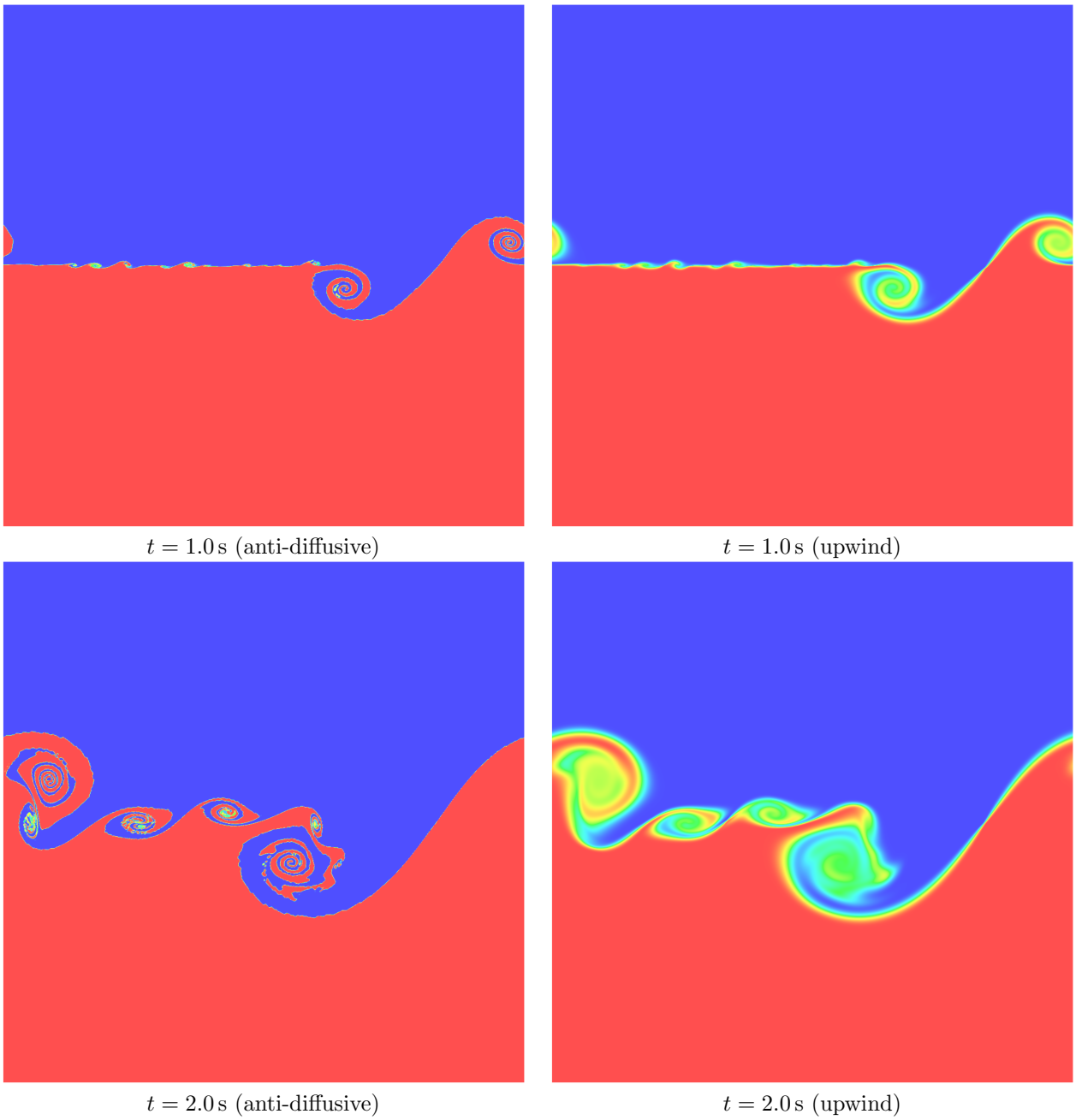

Figure 25: Kelvin-Helmoltz Instability Test. Mapping of the the color function values obtained with the anti-diffusive scheme and the upwind scheme at instants $t \in \{1.0, 2.0\}\,\mathrm{s}$.

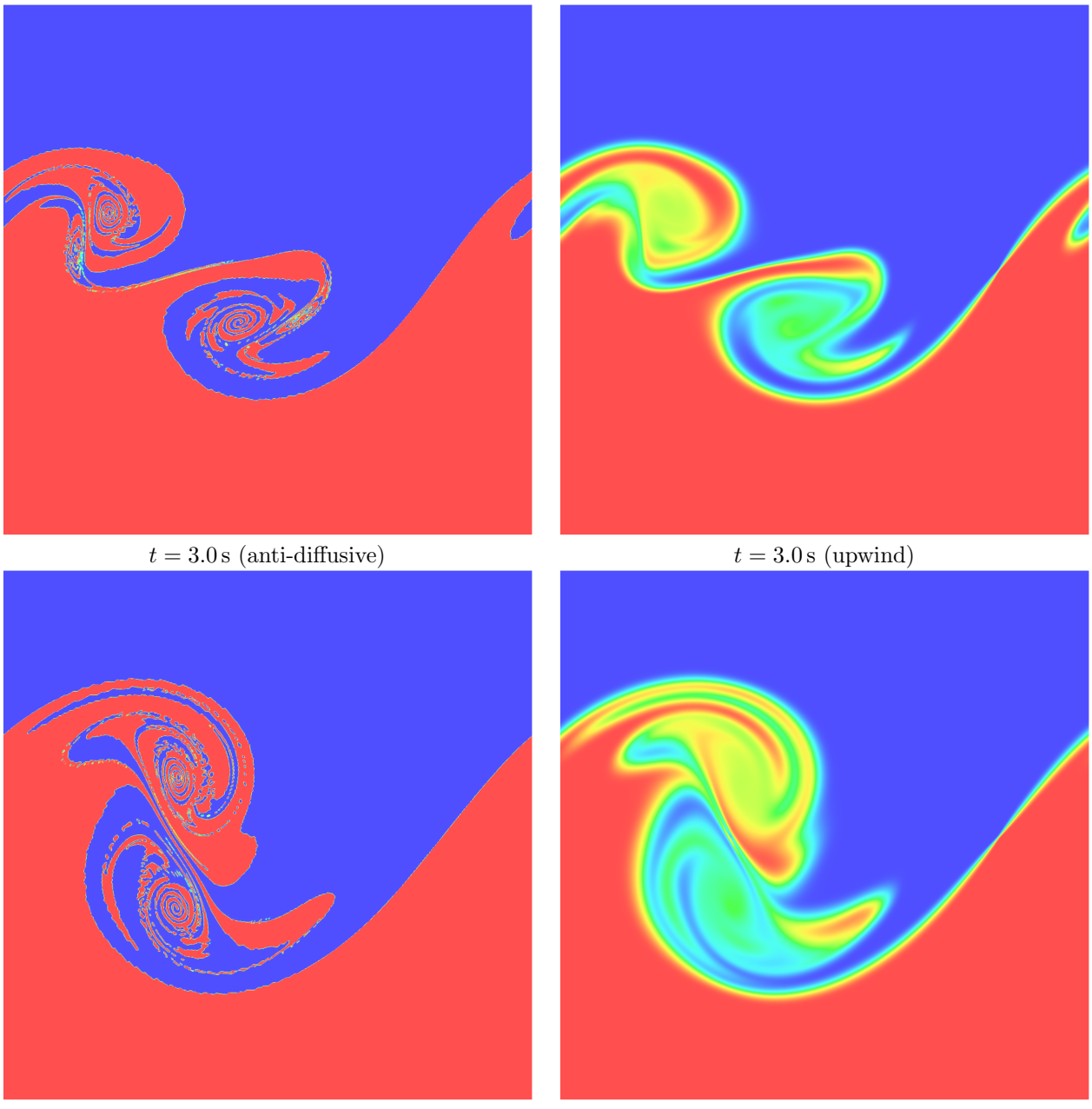

$t = 3.0\,\mathrm{s}$ (anti-diffusive) $t = 3.0\,\mathrm{s}$ (upwind)

$t = 4.0\,\mathrm{s}$ (anti-diffusive) $t = 4.0\,\mathrm{s}$ (upwind)

Figure 26: Kelvin-Helmoltz Instability Test. Mapping of the the color function values obtained with the anti-diffusive scheme and the upwind scheme at instants $t \in \{3.0, 4.0\}\,\mathrm{s}$.

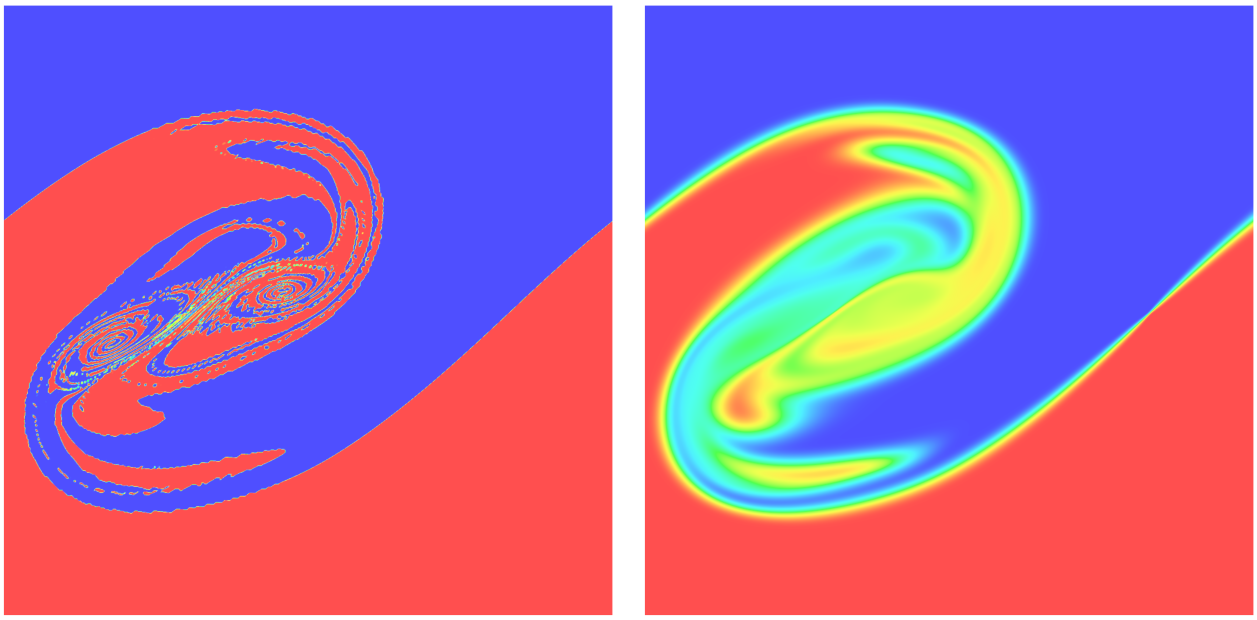

$t = 5.0\,\mathrm{s}$ (anti-diffusive)

$t = 5.0\,\mathrm{s}$ (upwind)

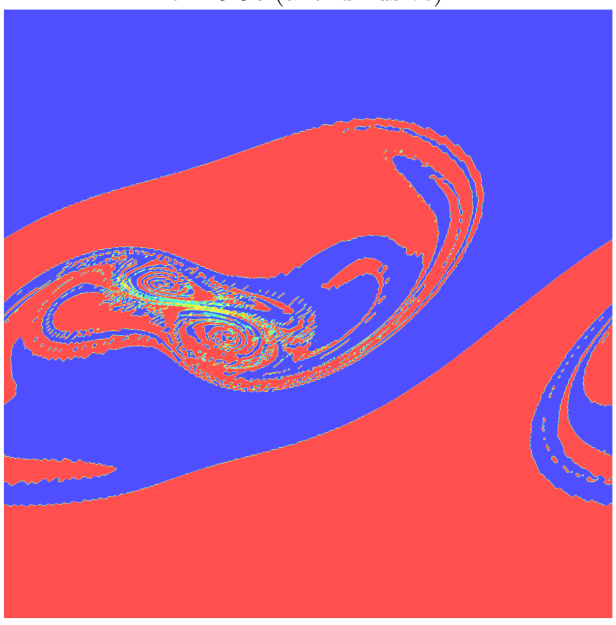

$t = 6.0\,\mathrm{s}$ (anti-diffusive)

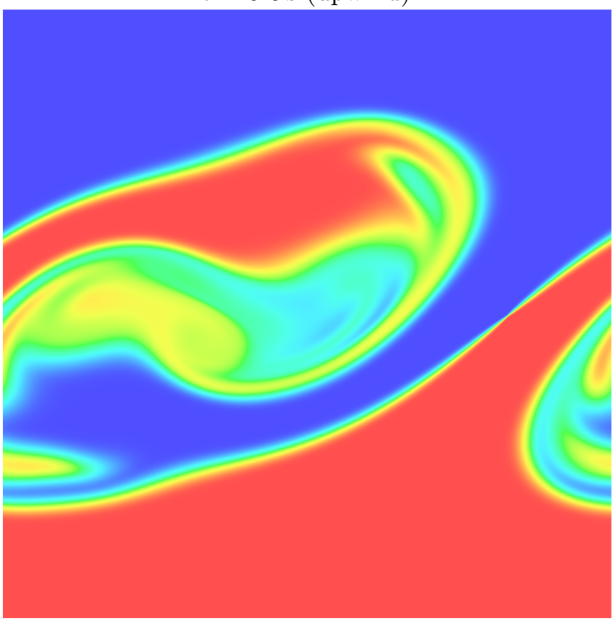

$t = 6.0\,\mathrm{s}$ (upwind)

Figure 27: Kelvin-Helmoltz Instability Test. Mapping of the the color function values obtained with the anti-diffusive scheme and the upwind scheme at instants $t \in \{5.0, 6.0\}\,\mathrm{s}$.

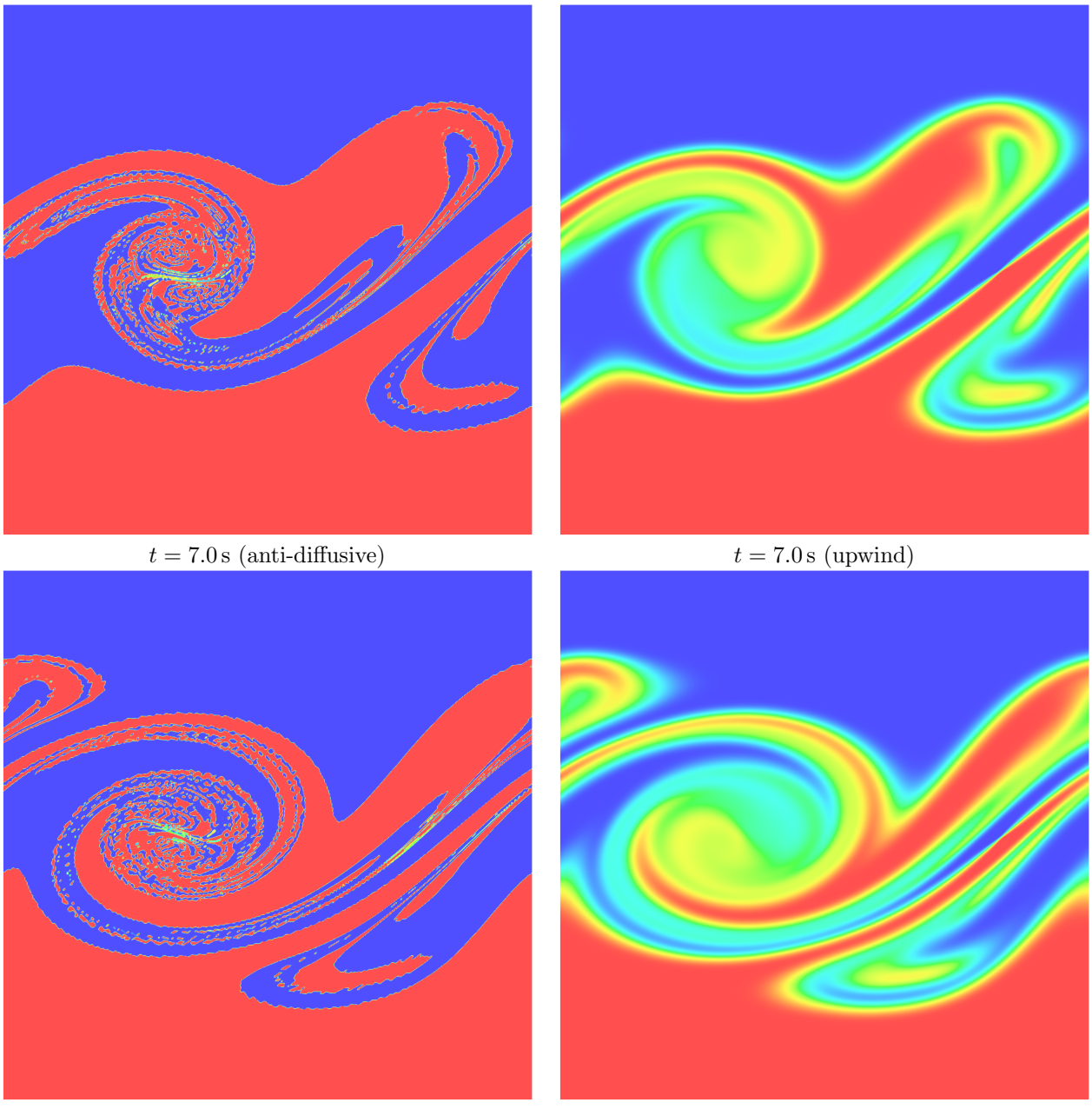

$t = 7.0\,\mathrm{s}$ (anti-diffusive) $t = 7.0\,\mathrm{s}$ (upwind)

$t = 8.0\,\mathrm{s}$ (anti-diffusive) $t = 8.0\,\mathrm{s}$ (upwind)

Figure 28: Kelvin-Helmoltz Instability Test. Mapping of the the color function values obtained with the anti-diffusive scheme and the upwind scheme at instants $t \in \{7.0, 8.0\}\,\mathrm{s}$.

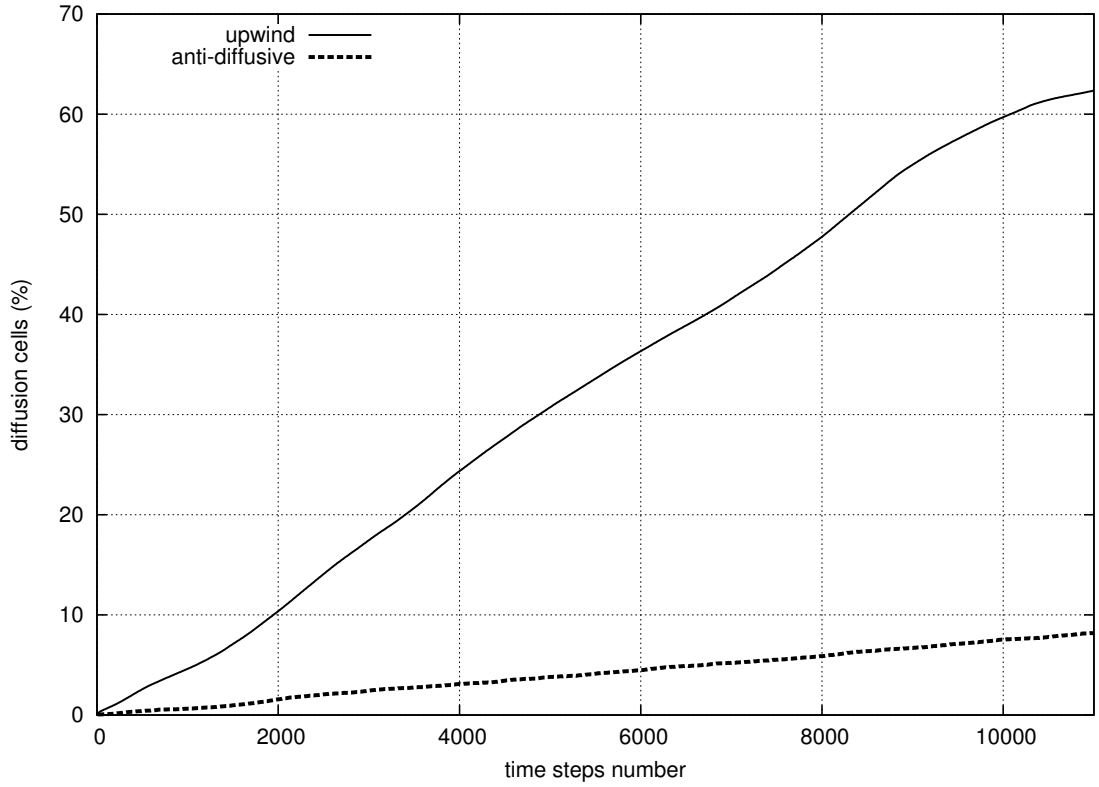

Figure 29: Kelvin Helmoltz Instability Test. Percent of cells in the domain where the color function z is numerically diffused versus the number of time steps, for both upwind and anti-diffusive scheme.

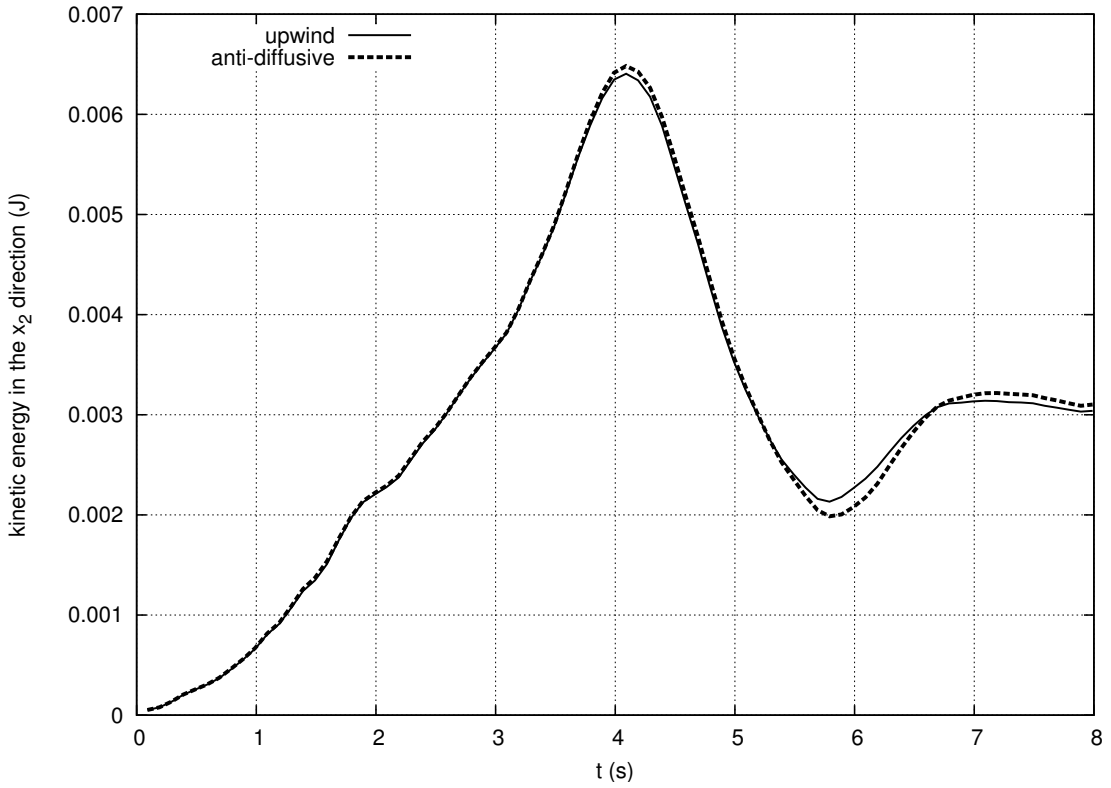

Figure 30: Kelvin Helmoltz Instability Test. Evolution of the kinetic energy in the direction x_2 throughout the computation in norm L^1: graph of the function $t \mapsto \int_{[0,1]\times[0,1]} \frac{1}{2}\rho u_2^2(x_1, x_2, t)\mathrm{d}x_1\mathrm{d}x_2$.